POLITECNICO DI TORINO

Master of Science in Energy and Nuclear Engineering

Master thesis

Novel TMPS structures for enhanced heat removal in divertor tiles for W7-X

Politecnico di Torino

Supervisors

Prof. Laura Savoldi

Dr. Joris Fellinger

Candidate

Alessio Quamori Tanzi

13th October 2023

Blank page

To my grandparents.

Abstract

To comply with the need for decarbonization of the power and industrial sector, the nuclear fusion Community is developing worldwide new advanced reactor designs to produce heat and/or electricity without emitting CO2. [4] In many of the different reactor designs, heat fluxes greater than 10 MW/m^2 are expected on some components such as the divertor, and must be properly exhausted. [19] The work presented in this thesis is focused on heat removal from the divertor. The aim is to design a new divertor module for the Wendelstein 7-X. equipped with Triply Periodic Minimal Surfaces (TPMS) to maximize heat transfer by promoting the mixing of the coolant in an extended heat transfer surface configuration. TPMS are three-dimensional surfaces that can be mathematically described by sinusoidal and cosinusoidal functions, from these surfaces periodic lattices can be generated. Considering the recent revolution in additive manufacturing, researchers started to investigate TPMS geometries that were impossible to manufacture by conventional manufacturing methods. [15] In the energy field, TPMS find applications as heat sinks in electronic devices or as heat exchangers. The TPMS structures are modeled using the software NTOPOLOGY. They can be chosen between gyroid, which has been intensively studied, and diamond which is expected to offer better thermal performance. The parameters of optimization involve variations in the structure type, orientation, and offset. The work begins with a parametric study with reduced domains, in order to find the best configuration (thickness + type of TPMS) that will be used to simulate the complete tile. The module is divided into eight identic tiles (100 mm x 300 mm x 5 mm) connected in parallel. Every tile is composed of a copper box plugged by a one-millimeter-thick tungsten lid. The TPMS structure is contained inside the box, and the water circulates through it. A one-millimeter soft-copper layer is inserted between the box and the tungsten layer to equalize the differences in the thermal expansion between copper and tungsten. The module can sustain a 15-bar pressure drop at most, with a 1.25 kg/s mass flow rate. The simulations are made using the Computational Fluid Dynamic software STAR-CCM+. As in most of the engineered interest cases, the Reynolds Averaged Navier-Stokes (RANS) equations are used as the turbulence model, with the SST $k - w$ (Shear Stress Transport) as the closure model. [17] Every material has its own constraints to respect: the temperature of the water must be lower than the saturation temperature, at the respective pressure, to avoid boiling. The copper temperature must be kept under 500 °C while the tungsten below 1200 °C. [18] A parametric study is made increasing the magnitude of the heat flux until one of the constraints is overcome. The results of the analysis, carried out in tight collaboration with the W7-X team at IPP in Greifswald, shows that selected TPMS can reach heat flux of 8 MW/m^2, becoming then an interesting option for the W7-X divertor tiles.

Table of Contents

Table of figures

List of tables

Chapter 1

1.1 Introduction

Energy is the base of modern societies. Aligned with the Paris Agreement, The European Green Deal has established the objectives to achieve CO2 neutrality by 2050, some investor guidelines have been set out through the green taxonomy to assist in making sustainable choices. [13]

Given that the energy sector is responsible for 40 % of the CO2 total emissions in the world [7], new clean energy sources are needed. The existing sources can be chosen between renewables, biomasses, nuclear power plants and others. For what regards nuclear, in 2021 the Joint Research Centre assessed nuclear energy in relation to the 'do not significant harm' criteria: the potential benefits of nuclear energy outweigh the associated risks. [1] The main challenge of the nuclear industry is to make sure nuclear energy is included among these sources.

Fusion energy is expected to be a very promising solution. The next generation fusion power reactors, like DEMO, are expected to operate in the second half of the century. [11] They will involve high power densities and they can generate heat fluxes that can range from 1 $\frac{MW}{m^2}$ to 20 $\frac{MW}{m^2}$ [9] therefore new heat sinks with high performances must be developed. Under operation conditions, the best heat sink is the one with the highest heat dissipation, the lowest pressure drop and with the least amount of material. [3] The traditional fin-shaped heat sinks like microchannels do not force the flow to change trajectory as it flows through the heat sink, thus their heat removal capabilities are limited. The aim is to find more complex geometries designed to introduce structure-driven enhanced turbulence. [20]

1.2 W7-X and its divertor

Wendelstein 7-X is the largest stellarator type fusion device currently operating in the world. Its objective is to investigate the suitability of this type for a power plant, comparable with a tokamak of the same size. It is composed of a system of 50 non-planar and 20 planar superconducting magnetic coils that produce an optimized magnetic field for confining the plasma. The main components are the magnetic coils, cryostat, plasma vessel, heating systems and the divertor. [12]

In 2022, after substituting the old uncooled graphite test divertor, it started plasma experiments with a water-cooled plasma-facing wall including a CFC based divertor. In 2021 was launched

another project to develop a W based divertor, that should retain small quantities of tritium. More specifically, WNiFe seems to be an interesting candidate as plasma-facing material due to its high ductility and its facility to machine. [10]

The divertor is made of units. Every unit is made of three vertical and nine horizontal target modules intersecting the strike lines. The modules consist of eight to twelve target elements (look to Figure 1). The unit is designed to have a pumping gap to pump out the neutrals, the efficiency of the neutral's removal depends on how much the field lines are closed to the pumping gap. [5]

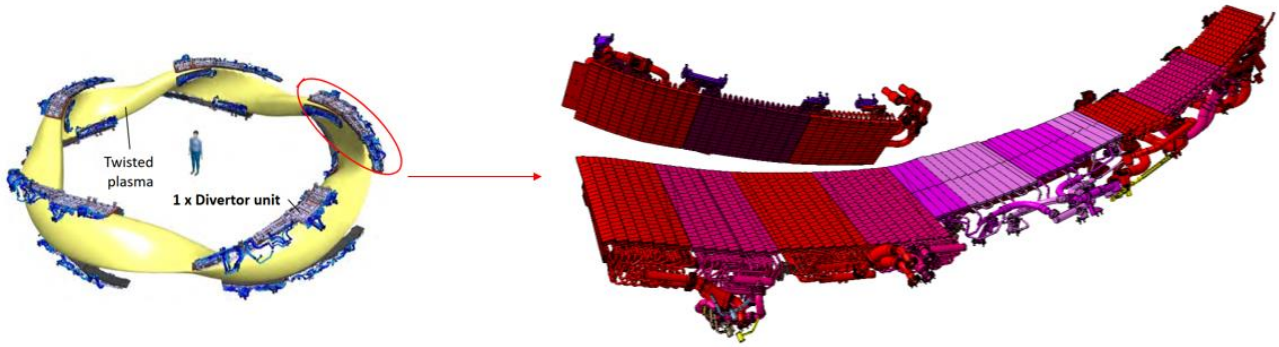

Figure 1: W7-X divertor

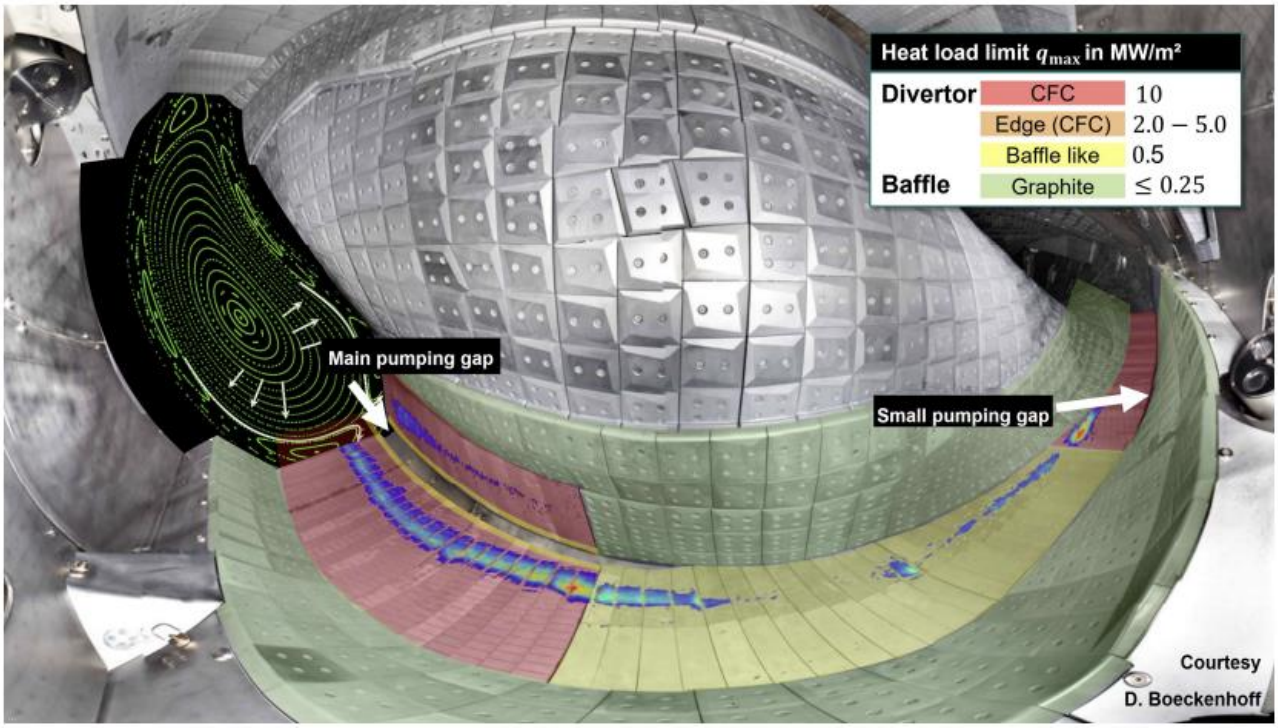

Figure 2: Interiors of the W7-X

1.3 TPMS

Considering the recent development in the additive manufacturing, also known as three-dimensional printing, new complex geometries like TPMS can be easily fabricated without involving milling, drilling or casting.

TPMS have been discovered in the 19th century. They are geometrically complex surfaces with a large area to volume ratio and smooth surfaces. They are expected to guarantee high heat dissipation, contained pressure drop and a reduced weight. Due to these features, they are an interesting candidate to be used in the next generation heat sinks. [2]

TPMS can be derived mathematically using trigonometric functions that describe an isosurface evaluated at an isovalue *c*. The value of *c* controls the morphology of the surface. In equation (1) and equation (2) are reported the equations for the two well-known Schwarz Diamond and Schwarz Gyroid minimal surfaces.

$$Gyroid \rightarrow \sin x \cos y + \sin y \cos z + \sin z \cos x = c \quad (1)$$

$$Diamond \rightarrow cosx \cos y \cos z - \sin x \sin y \sin z = c \quad (2)$$

Where x, y and z are the Cartesian coordinates and c is the isovalue. [2]

The topology of the minimal surface can be controlled by following two strategies named the solid-networks and the sheet-networks. In the first one the volume enclosed by the minimal surface at a certain isovalue *c* is solidified. Instead, the sheet-network structure is obtained by solidifying the volume enclosed by the intersection of two isosurfaces evaluated at $\pm c$. The two different strategies are depicted in Figure 3.

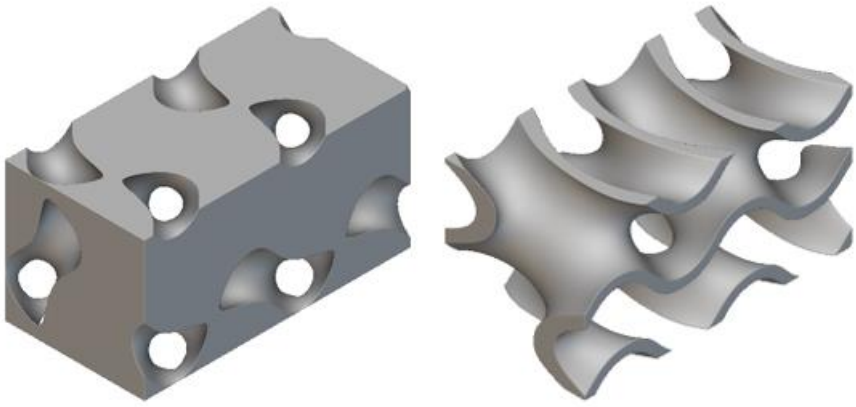

Figure 3: Solid-networks on the left, sheet-networks on the right

In this work, only the sheet-networks strategy has been used.

1.4 Objective of the work

The following work wants to investigate the thermal-hydraulic performances of the Schwarz Gyroid and Schwarz Diamond minimal surfaces with a sheet topology. The proposal that can support the higher imposed heat flux will be identified as the best option. This one will be then used in a bigger design that simulates the TPMS-based divertor target of the W7-X.

Chapter 2: Development of a TPMS-based tile

2.1 Rationale

This Chapter is devoted to the development of a TPMS-based tile.

The choice of TPMS is crucial to obtain a tile with the best thermal performances possible. The choice can be between *Gyroid, Diamond, Lidinoid* and *SplitP* because are the types of TPMS that can be generated by the software *Ntopology*. Every TPMS can be generated with a unit cell size and a wall thickness (and consequently a porosity), so it is easy to understand that the generated TPMS can have different heat removal capabilities and different pressure drops depending on the choice of these parameters. Considering that *Gyroid* and *Diamond* are easier to be meshed, in the following will be considered only these two types of TPMS.

Every TPMS can be generated choosing among three different wall thickness ($0.8\ mm, 1\ mm, 1.2\ mm$) and two unit-cell sizes ($10\ mm \times 10\ mm \times 5\ mm\ and\ 10\ mm \times 10\ mm \times 10\ mm$). All the combinations are simulated inside two small domains of dimensions $10mm \times 20mm \times 5mm$ and $10mm \times 20mm \times 10mm$, for a total of twelve combinations. The assembling procedure and the simulation setup are explained in Chapter 3. The TPMS (with respective unit cell size and wall thickness) that can sustain the highest heat flux (call it '*heat flux small*') will be used inside the TPMS-based tile as explained in Chapter 4. In conclusion, is checked if the maximum heat flux sustained by the tile is equal to '*heat flux small*'.

To facilitate the comprehension a flow chart is shown in Figure 4.

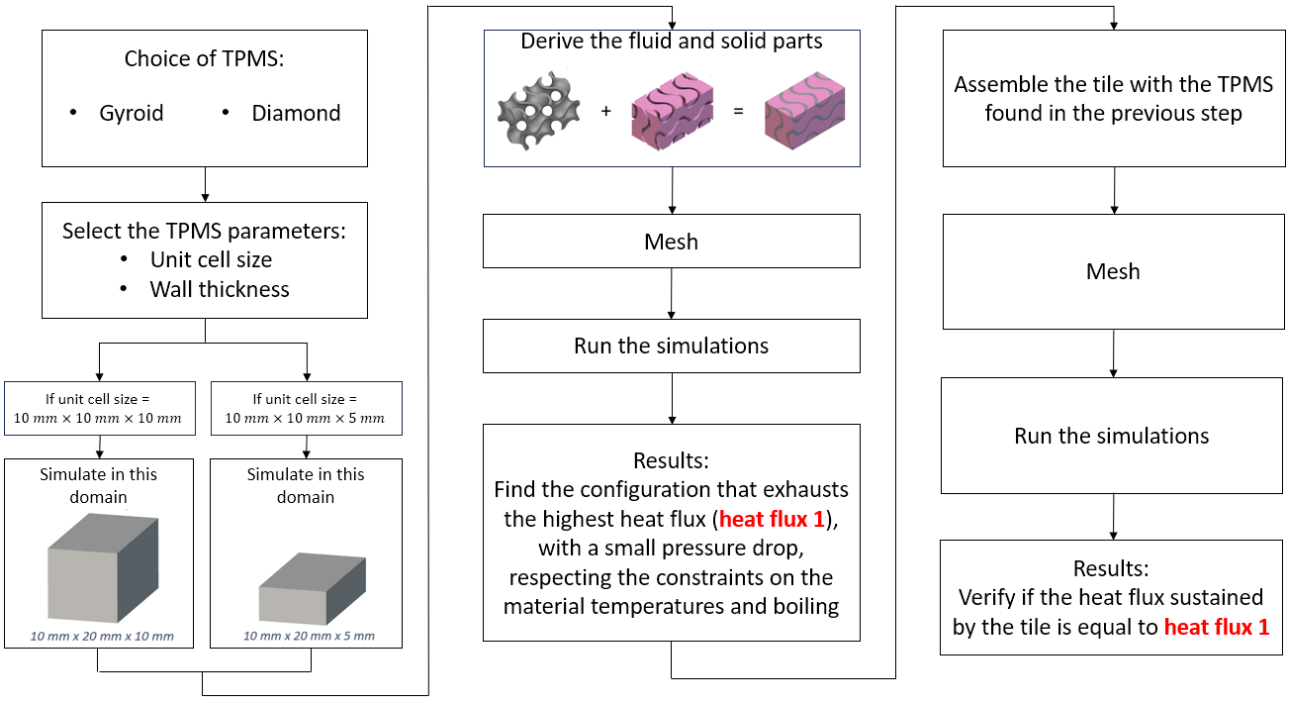

Figure 4: Flow chart

2.2 Configurations

The TPMSs are tested in two types of parallelepipedal domains, with dimensions $10mm \times 20mm \times 5mm$ and $10mm \times 20mm \times 10mm$. The domains are depicted in Figure 5 and Figure 6. In one domain are inserted two unit cells:

- the domain $10mm \times 20mm \times 5mm$ is composed of two unit cells with dimensions $10mm \times 10mm \times 5mm$.
- the domain $10mm \times 20mm \times 10mm$ is composed of two unit cells with dimensions $10mm \times 10mm \times 10mm$.

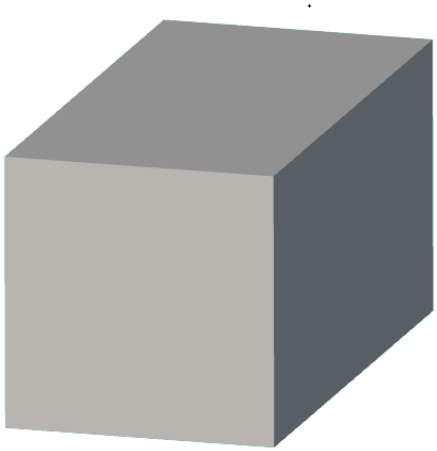

Figure 5: 10 mm x 20 mm x 10 mm domain

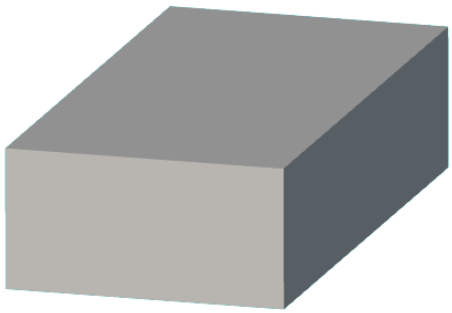

Figure 6: 10 mm x 20 mm x 5 mm domain

Since two types of TPMS are investigated in two domains, and they can be originated by choosing among three wall thicknesses, twelve total cases will be simulated.

Given a TPMS, the wall thickness is the key parameter to vary the volume occupied by the solid (and so by the fluid), in other words, the porosity is a function of the wall thickness.

From Table 1 to Table 4 are reported the volume of the solid, volume of the fluid and the wall surface of the Schwarz Gyroid and the Schwarz Diamond for different values of the wall thickness.

Wall thickness [mm]	Surface [mm^2]	Solid volume [mm^3]	Fluid volume [mm^3]
0,8	2034,81	450,17	2090,83
1	2049	563,17	1977,83
1,2	2082,79	677,19	1863,81

Table 1: Wall thickness, Surface, Solid volume and Fluid volume for a Diamond TPMS with unit cell size 10 mm x 10 mm x 10 mm

Wall thickness [mm]	Surface [mm^2]	Solid volume [mm^3]	Fluid volume [mm^3]
0,8	1619,54	311,67	1074,33
1	1666,79	391,27	994,73
1,2	1695,49	471,77	914,23

Table 2: Wall thickness, Surface, Solid volume and Fluid volume for a Diamond TPMS with unit cell size 10 mm x 10 mm x 5 mm

Wall thickness [mm]	Surface [mm^2]	Solid volume [mm^3]	Fluid volume [mm^3]
0,8	1647,6	379,8	2161,2
1	1674,2	475,5	2065,5
1,2	1717	571,3	1969,7

Table 3: Wall thickness, Surface, Solid volume and Fluid volume for a Gyroid TPMS with unit cell size 10 mm x 10 mm x 10 mm

Wall thickness [mm]	Surface [mm^2]	Solid volume [mm^3]	Fluid volume [mm^3]
0,8	1344,51	264,27	1121,73
1	1383,58	331,65	1054,35
1,2	1420,5	399,68	986,32

Table 4: Wall thickness, Surface, Solid volume and Fluid volume for a Gyroid TPMS with unit cell size 10 mm x 10 mm x 5 mm

From Table 5 to Table 8 is appreciable how the porosity changes with the wall thickness.

Wall thickness [mm]	S/V_s [$^1/_m$]	S/V_f [$^1/_m$]	$Porosity$ [%]
0,8	4,52	0,97	54,98
1	3,63	1,03	43,68
1,2	3,07	1,11	32,28

Table 5: Surface over volume ratio and porosity for a Diamond TPMS with unit cell size 10 mm x 10 mm x 10 mm

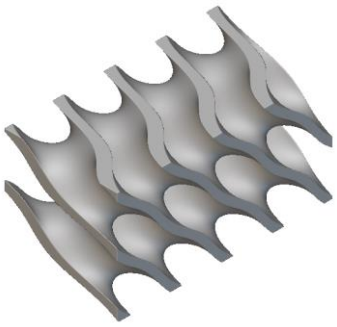

Figure 7: Diamond in a 10 mm x 20 mm x 10 mm domain

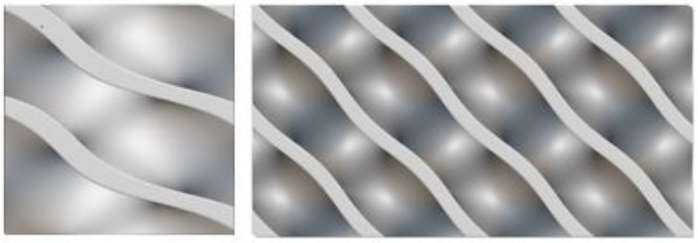

Figure 8: Frontal and lateral view of the Diamond in a 10 mm x 20 mm x 10 mm domain

Wall thickness $[mm]$	S/V_s $[1/m]$	S/V_f $[1/m]$	$Porosity$ [%]
0,8	5,19	1,50	68,83
1	4,25	1,67	60,87
1,2	3,59	1,85	52,82

Table 6: Surface over volume ratio and porosity for a Diamond TPMS with unit cell size 10 mm x 10 mm x 5 mm

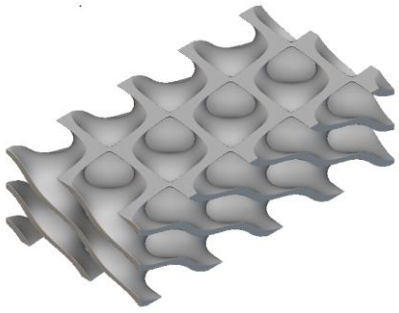

Figure 9: Diamond in a 10 mm x 20 mm x 5 mm domain

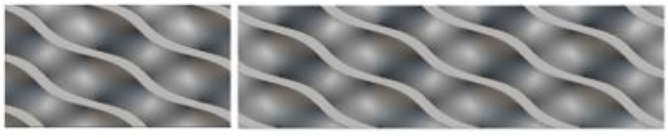

Figure 10: Frontal and lateral view of the Diamond in a 10 mm x 20 mm x 5 mm domain

Wall thickness [mm]	S/V_s [$^1/_m$]	S/V_f [$^1/_m$]	$Porosity$ [%]
0,8	4,33	0,76	81,01
1	3,52	0,81	76,22
1,2	3,00	0,87	71,43

Table 7: Surface over volume ratio and porosity for a Gyroid TPMS with unit cell size 10 mm x 10 mm x 10 mm

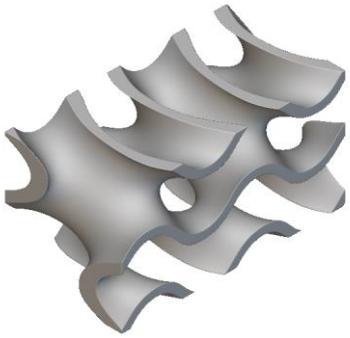

Figure 11: Gyroid in a 10mm x 20mm x 10mm domain

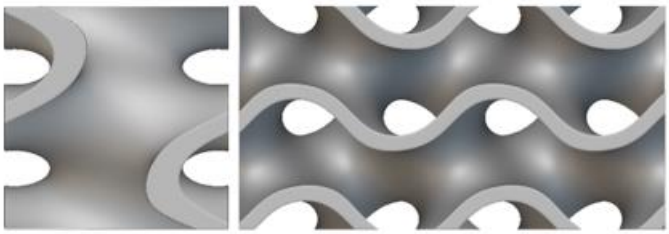

Figure 12: Frontal and lateral view of the Gyroid in a 10mm x 20mm x 10mm domain

Wall thickness [mm]	S/V_s [$^1/_m$]	S/V_f [$^1/_m$]	$Porosity$ [%]
0,8	5,08	1,19	73,57
1	4,17	1,31	66,83
1,2	3,55	1,44	60,03

Table 8: Surface over volume ratio and porosity for a Gyroid TPMS with unit cell size 10 mm x 10 mm x 5 mm

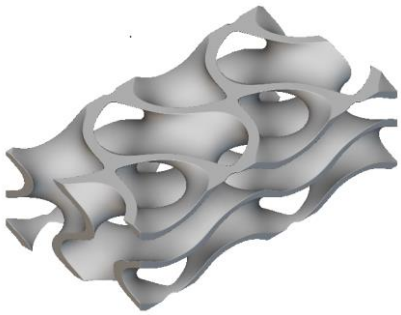

Figure 13: Gyroid in a 10mm x 20mm x 5mm domain

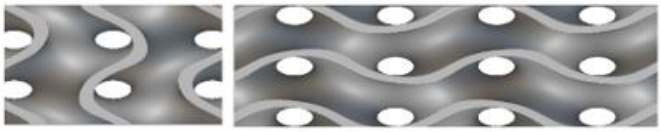

Figure 14: Frontal and lateral view of the Gyroid in a 10 mm x 20mm x 5mm domain

For clarity, the $\frac{surface}{volume_{fluid}}$ as a function of the wall thickness for different type pf TPMS, is shown in Figure 15. At the same way, the $\frac{surface}{volume_{solid}}$ as a function of the wall thickness is shown in Figure 16.

The configurations with highest $\frac{surface}{volume_{fluid}}$ are the Gyroid and Diamond inserted in the smaller domain ($10mm \times 20mm \times 5mm$), so given a domain, they guarantee more surface that interfaces with the fluid. For this reason, they are probably the most promising ones.

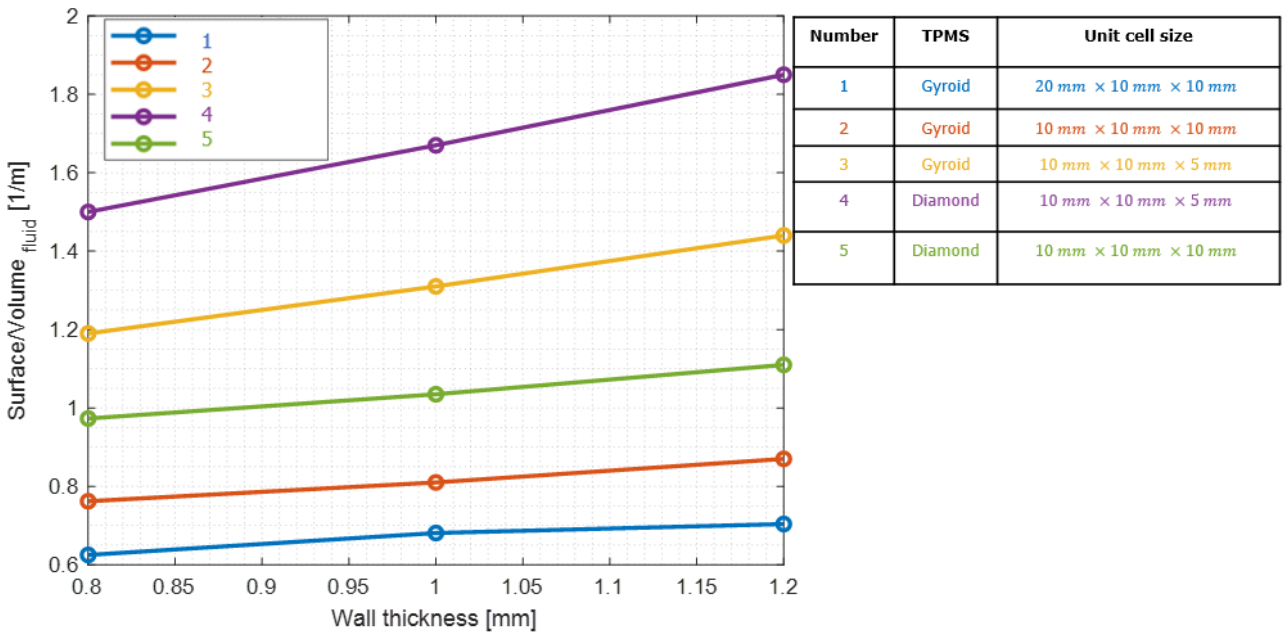

Number	TPMS	Unit cell size
1	Gyroid	$20\ mm \times 10\ mm \times 10\ mm$
2	Gyroid	$10\ mm \times 10\ mm \times 10\ mm$
3	Gyroid	$10\ mm \times 10\ mm \times 5\ mm$
4	Diamond	$10\ mm \times 10\ mm \times 5\ mm$
5	Diamond	$10\ mm \times 10\ mm \times 10\ mm$

Figure 15: $\frac{surface}{volume_{fluid}}$ as a function of the wall thickness.

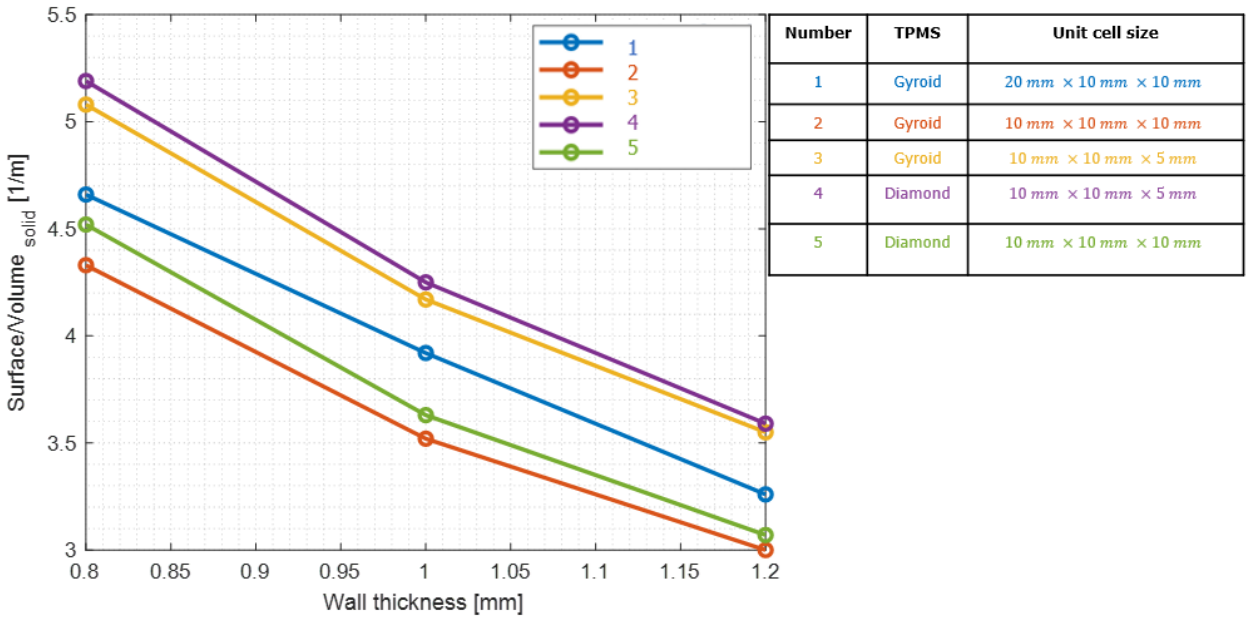

Number	TPMS	Unit cell size
1	Gyroid	$20\ mm \times 10\ mm \times 10\ mm$
2	Gyroid	$10\ mm \times 10\ mm \times 10\ mm$
3	Gyroid	$10\ mm \times 10\ mm \times 5\ mm$
4	Diamond	$10\ mm \times 10\ mm \times 5\ mm$
5	Diamond	$10\ mm \times 10\ mm \times 10\ mm$

Figure 16: $\frac{surface}{volume_{solid}}$ as a function of the wall thickness

Chapter 3: Model for the unit cell

3.1 Simulation setup

Regions and materials

In this section is explained how the simulation regions are assembled. The fluid regions, shown in pink, are obtained with a subtract operation between the Gyroid and Schwarz-Diamond structures and the two basic volumes of Figure 5 and Figure 6. In the following figures is shown the assemblage of all the cases with $1\ mm$ wall thickness.

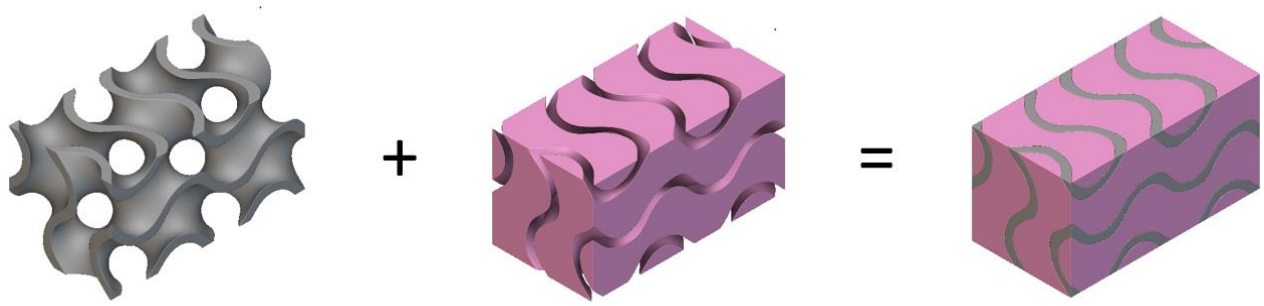

Figure 17: Regions assemblage for the Gyroid in a 10mm x 20mm x 10mm domain

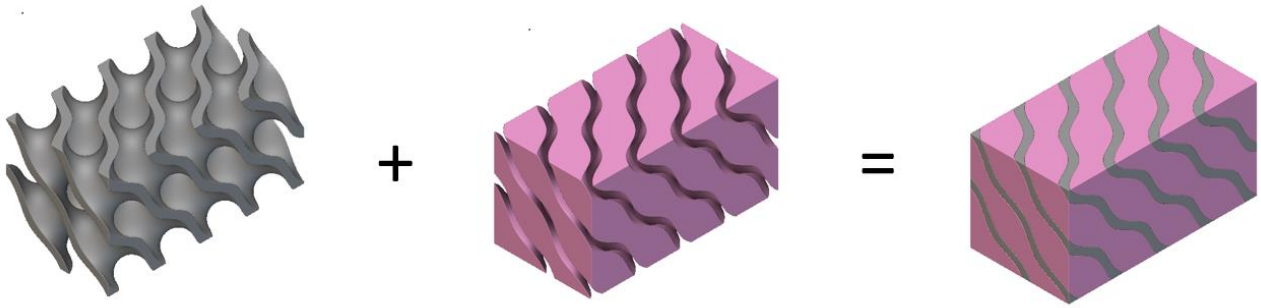

Figure 18: Regions assemblage for the Diamond in a 10mm x 20mm x 10mm domain

Figure 19: Regions assemblage for the Gyroid in a 10 mm x 20mm x 5mm domain

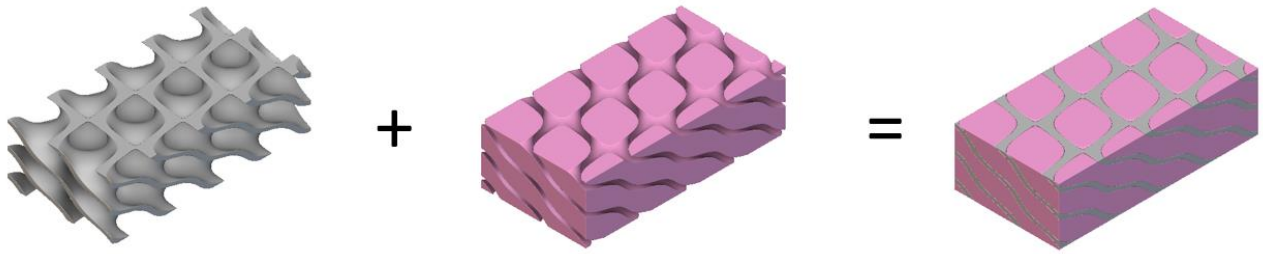

Figure 20: Regions assemblage for the Diamond in a 10 mm x 20mm x 5mm domain

Upon these domains, two layers with a thickness of 1 millimeter are added as shown in Figure 21. The brown layer is made of soft copper, while the grey layer is tungsten. Their properties are resumed in Table 11 and Table 12.

As a preliminary analysis, all the properties reported in the following are considered not dependent from the temperature. Future works will also include temperature dependent properties.

The fluid used is common water, which properties are shown in the following table.

Property	**Value**
$Density\ [\frac{kg}{m^3}]$	997,5
$Dynamic\ Viscosity\ [Pa \cdot s]$	$8{,}887e-4$
$Specific\ heat\ [\frac{J}{kg \cdot K}]$	4181,72
$Thermal\ conductivity\ [\frac{W}{m \cdot K}]$	0,62

Table 9: Water properties

The TPMS are made of a CuCrZr (Copper-Cromium-Zirconium) alloy which properties are in Table 10.

Property	Value
$Density\ [\frac{kg}{m^3}]$	8800
$Specific\ heat\ [\frac{J}{kg \cdot K}]$	410
$Thermal\ conductivity\ [\frac{W}{m \cdot K}]$	340

Table 10: CuCrZr properties

Property	Value
$Density\ [\frac{kg}{m^3}]$	8800
$Specific\ heat\ [\frac{J}{kg \cdot K}]$	410
$Thermal\ conductivity\ [\frac{W}{m \cdot K}]$	340

Table 11: Soft Copper properties

Property	Value
$Density\ [\frac{kg}{m^3}]$	19300
$Specific\ heat\ [\frac{J}{kg \cdot K}]$	134
$Thermal\ conductivity\ [\frac{W}{m \cdot K}]$	163,2

Table 12: Tungsten properties

In Figure 21 is shown the final configuration, ready to be meshed.

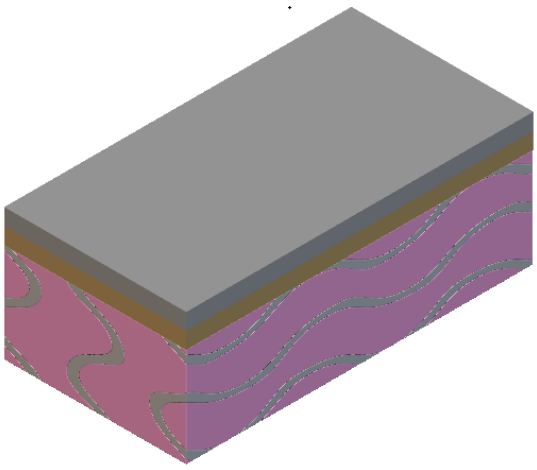

Figure 21: Reduced domain ready to be meshed

Boundary conditions

Every case has the same boundary conditions, a mass flow rate of $0.1\ kg/s$ at the inlet and an imposed pressure of $10\ bar$ at the outlet, with symmetry conditions on the lateral sides. On the top side of the tungsten layer the heat flux can be imposed.

The value of the mass flow rate is evaluated considering that in the tile of the divertor target, considering the available pumps, can be only circulated a mass flow rate up to $1.25\ kg/s$. The ratio of the frontal area of the reduced domains with respect to that of the tile is $\frac{1}{10}$, consequently, the tenth of $1.25\ kg/s$ is the value of the inlet mass flow rate.

3.2 Turbulence model and wall treatment

There are different approaches to the numerical solution of turbulence. In most of the cases of engineering interest, the Reynolds Averaged Navier-Stokes (RANS) equations are used. RANS only solve the mean flow, not considering even large eddies. Other models (LES and DNS) may be for sure more accurate, but they are also much more difficult to implement and computationally more expensive than RANS. Thus, in this section (and in the CFD simulations that are the object of the present work) only RANS models are considered. According to the number and type of the equations that are added, different turbulence closure models can be adopted. The main ones are the k −ϵ and the k − ω models. The k −ϵ model adds two equations: one for the turbulent kinetic energy k and one for the rate of dissipation of the turbulent kinetic energy per unit mass ϵ. This model is widely used and studied, and it is probably the most robust among the different possibilities. Even though the k − ϵ model is quite good far from the walls, it is not accurate in situations that involve high pressure gradients, complex geometries, separation of the flow and strong curvature of the streamlines, so it is not appropriate for TPMSs. The k − ω is also a two equations model, instead of ϵ, it uses the turbulence frequency ω = ϵ/k. It performs well in the near wall region and more poorly far from the wall. An intermediate model can be used: the SST k −ω. It combines the advantages of the previous models to have a good performance both near and far from the wall. It is similar to the k − ϵ model in the bulk of the flow and to the k − ω near the boundaries. As far as the numerical wall treatment is concerned, in most of CFD codes such as Star CCM+, a choice can be made between Low, High and All y+. In the simulations of this work an All y+ approach has been adopted.

3.3 Mesh

A 2D Automated Mesh was produced for the solution of the problem in analysis. For a good generation of the mesh, the polygonal and prism layer meshers have been selected. Polygonal cells have many neighbors (this leads to a better representation of gradients) and they require a lower computational cost. In turbulent regime, in the region where the fluid meets the boundary, large velocity gradients in the direction perpendicular to the wall are expected because of eddies and no slip condition. To correctly evaluate the velocity and temperature fields in this region, prism layers are used. The prism layers are well refined in the perpendicular direction while the cell size parallel to the surface is large enough to avoid excessive cell counts. When choosing the number of prism layers, their growth rate and the total thickness different aspects need to be considered. The dimension of the last prism layer (the farther from the wall) should be comparable with the size of the adjacent cells. This can be regulated with a correct combination of total prisms thickness and number of layers. The thickness of the first layer (near wall) directly influences the y+ of the first cell. Considering the All y+ approach, its value should be included between 1 and 5. [16]

The mesh parameters are resumed in Table 13.

$Base\ size\ [mm]$	$Number\ of\ prism\ layers\ [mm]$	$Prism\ layer\ near\ wall\ thickness\ [m]$	$Prism\ layer\ total\ thickness\ [mm]$
0.5	5	1E-5	0.2

Table 13: mesh parameters

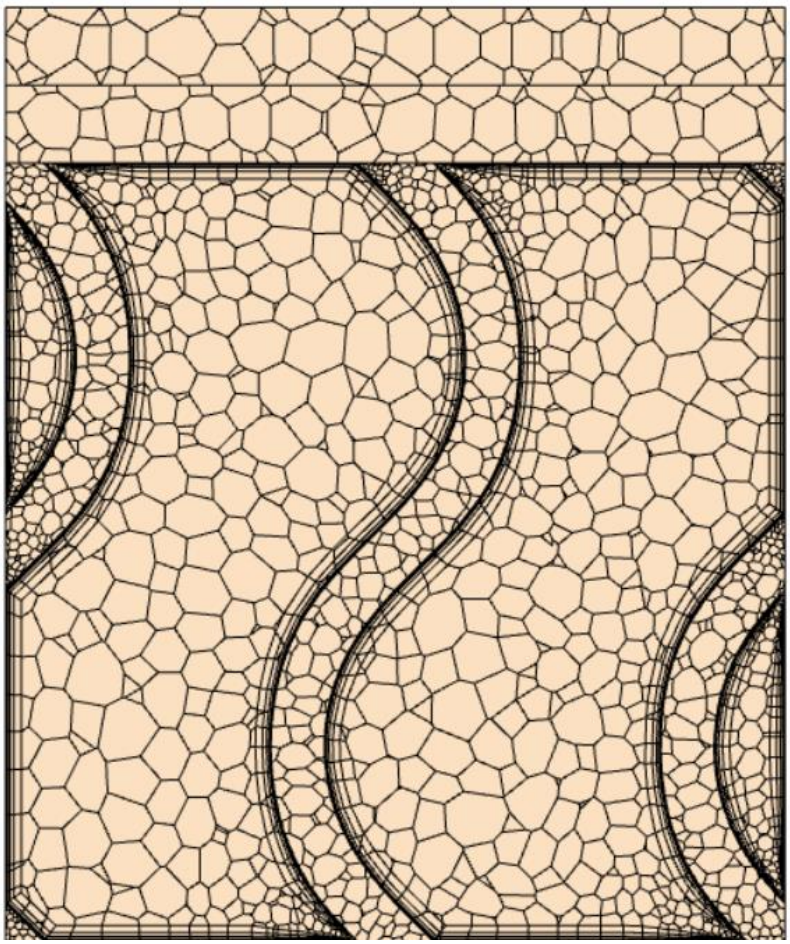

Figure 22: Frontal view of the mesh in the 10 mm × 20 mm × 10 mm domain

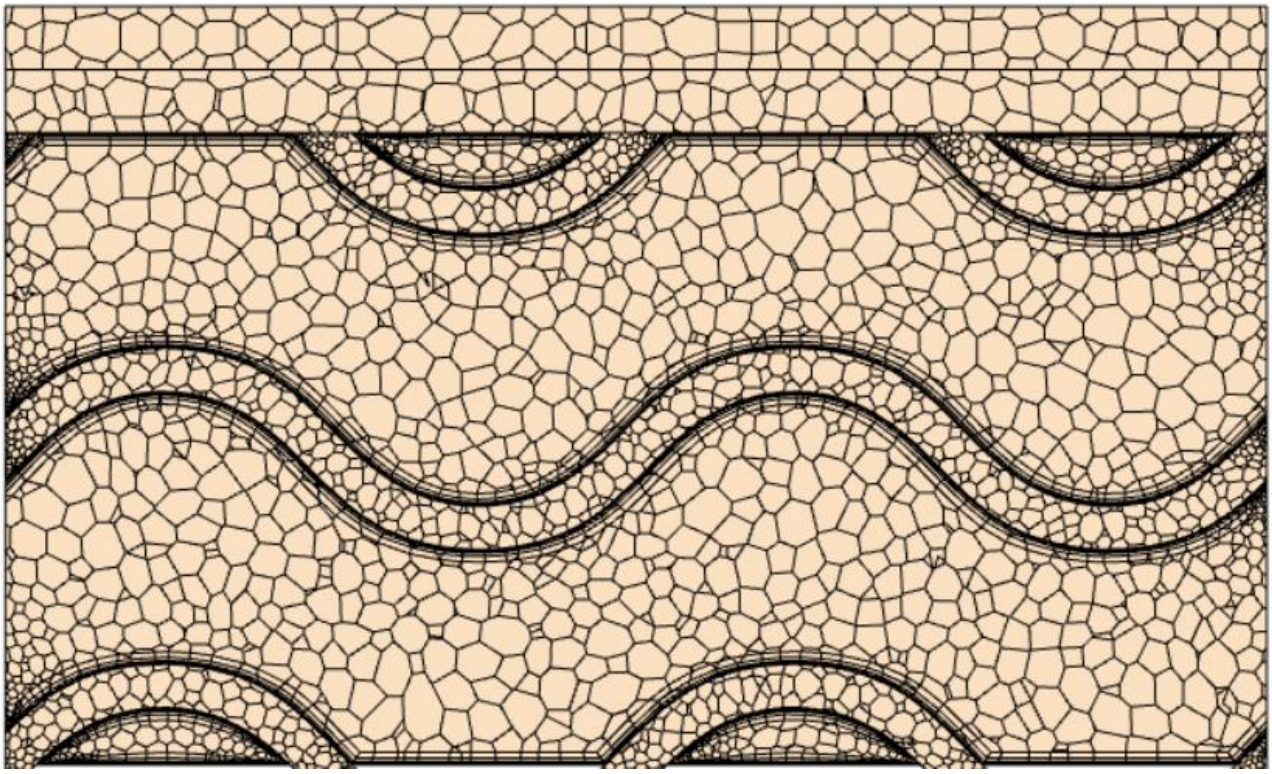

Figure 23: Lateral view of the mesh in the 10 mm × 20 mm × 10 mm domain.

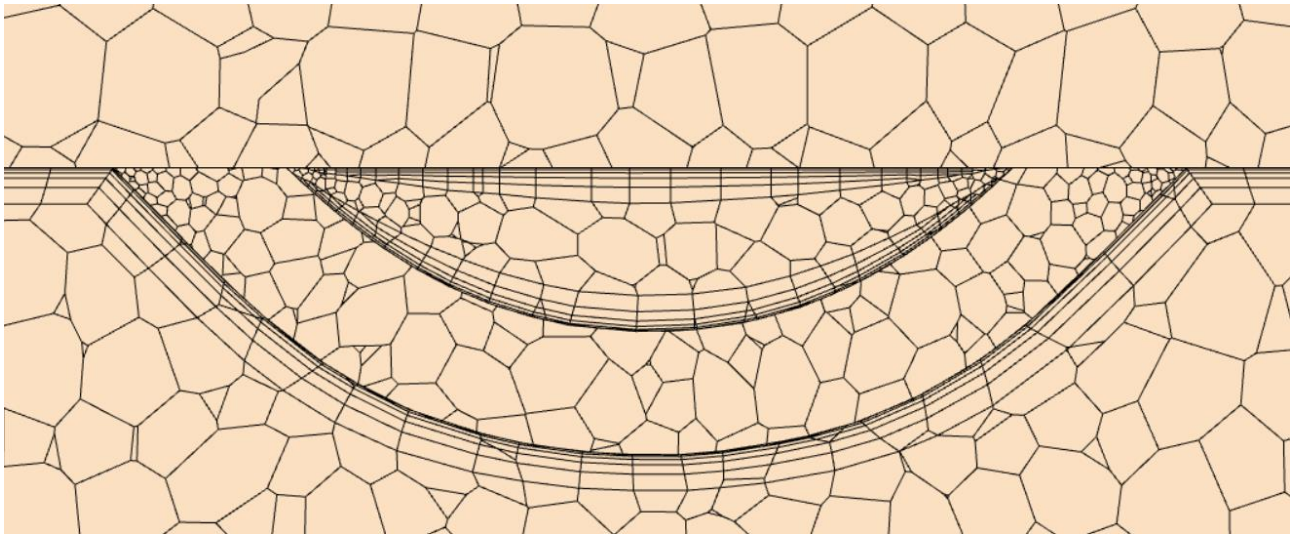

Figure 24: Zoomed view of the mesh in the 10 mm × 20 mm × 10 mm domain.

The quality of the mesh could be better near the angles, the prism layers tend to reduce their thickness or sometimes even disappear in that region. Since the following study doesn't want to investigate the heat transfer coefficient or quantities near the wall region, the error can be considered, in first approximation, acceptable. The dimension of the cells in the soft copper layer is bigger than in the TPMS region because the mesh operation has been carried out as a Per-Part based operation, so the software meshes the regions separately, this behavior could induce errors in the results but simplifies the simulation. Moreover, the number of prism layers could be increased, five prism layers are a good starting point, but in further works could also be used eight or more prism layers, also including an independence analysis.

3.4 Simulations

To help the convergence of the residuals the simulations are firstly run only hydraulically and then thermically.

As said before, the hydraulic simulation consists of a mass flow rate of $0.1\ kg/s$ at the inlet and a pressure of $10\ bar$ at the outlet, with symmetry conditions on the lateral sides. Once the hydraulic residuals reach low values, the energy equations are added to the simulations and the heat flux on the top of the tungsten layer is imposed. The simulation is stopped when the residuals converge.

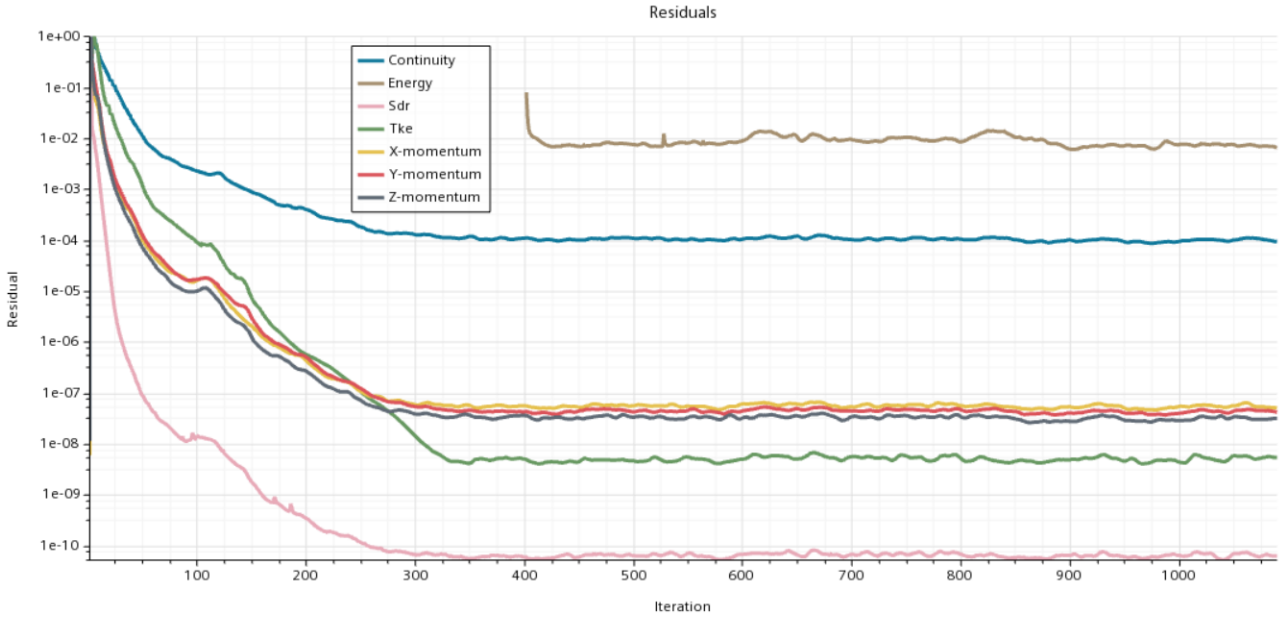

Figure 25: Residuals convergence

3.5 Results

Hydraulic results

In this section the hydraulic results of the small domains are shown.

The velocity field is shown on a cross and longitudinal sections to better visualize the internal structure. In general, configurations with bigger wall thickness produce higher values of velocity. In the following the velocity scene in shown for all the twelve combinations.

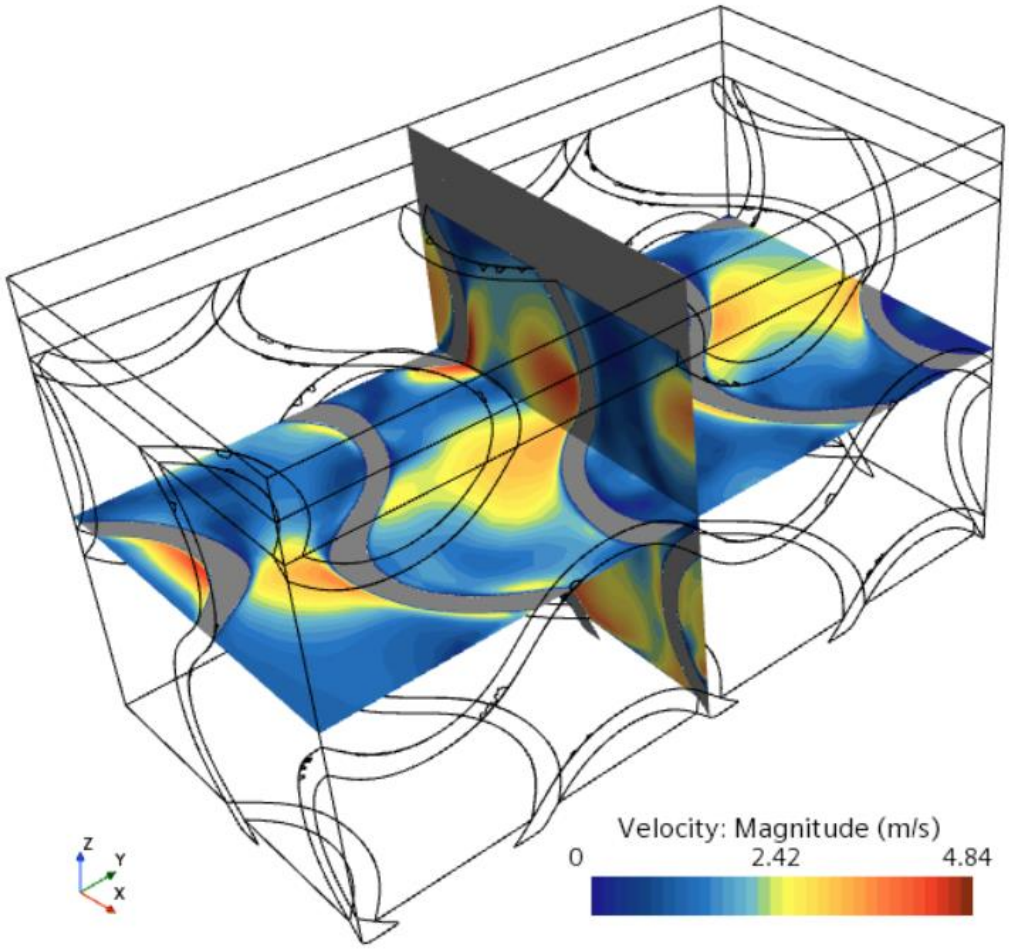

Figure 26: Velocity scene of a Gyroid with 0.8 mm wall thickness in a 10mm x 20mm x 10 mm domain

In Figure 26 is shown the velocity scene of a *Gyroid* with $0.8\,mm$ wall thickness in a $10\,mm \times 20\,mm \times 10\,mm$ domain. The velocity of water near the upper wall is very low, so it is expected to have reduced heat removal performances.

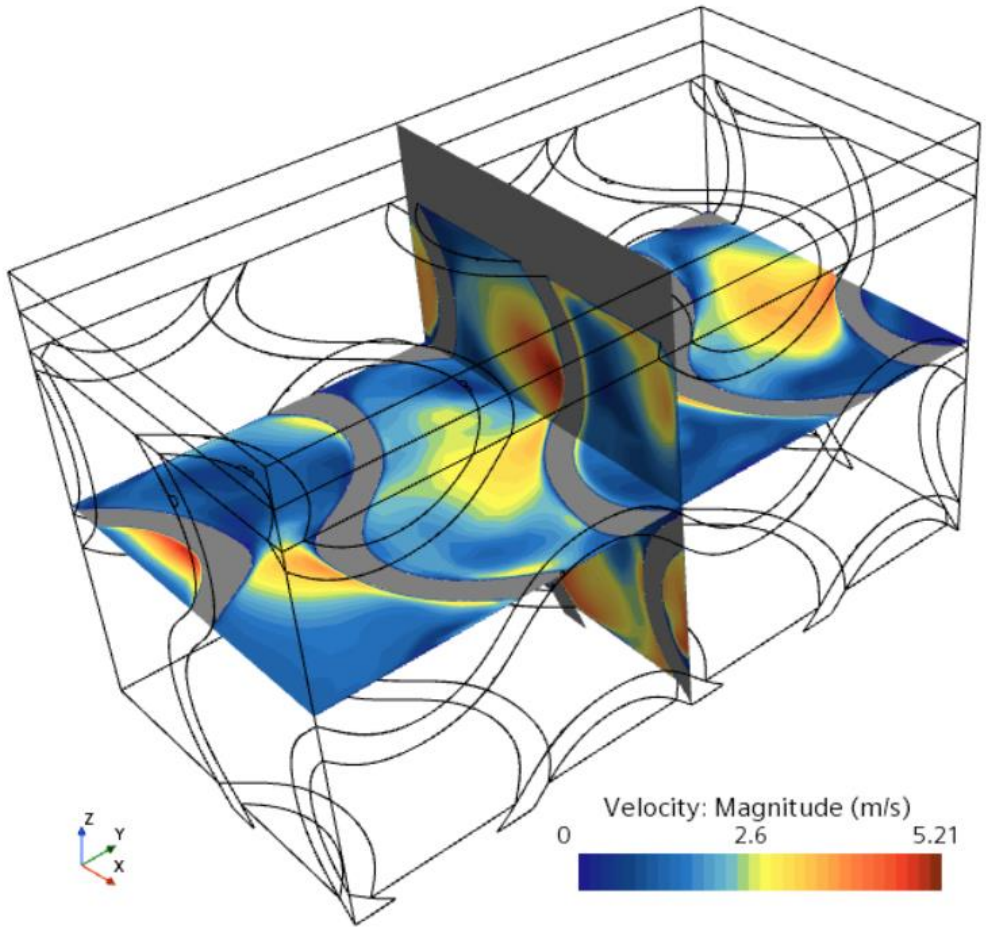

Figure 27: Velocity scene of a Gyroid with 1 mm wall thickness in a 10mm x 20mm x 10 mm domain

In Figure 27 is shown the velocity scene of a *Gyroid* with $1\,mm$ wall thickness in a $10\,mm \times 20\,mm \times 10\,mm$ domain. The velocity of water near the upper wall is very low, so as the previous case, it is expected to have reduced heat removal performances.

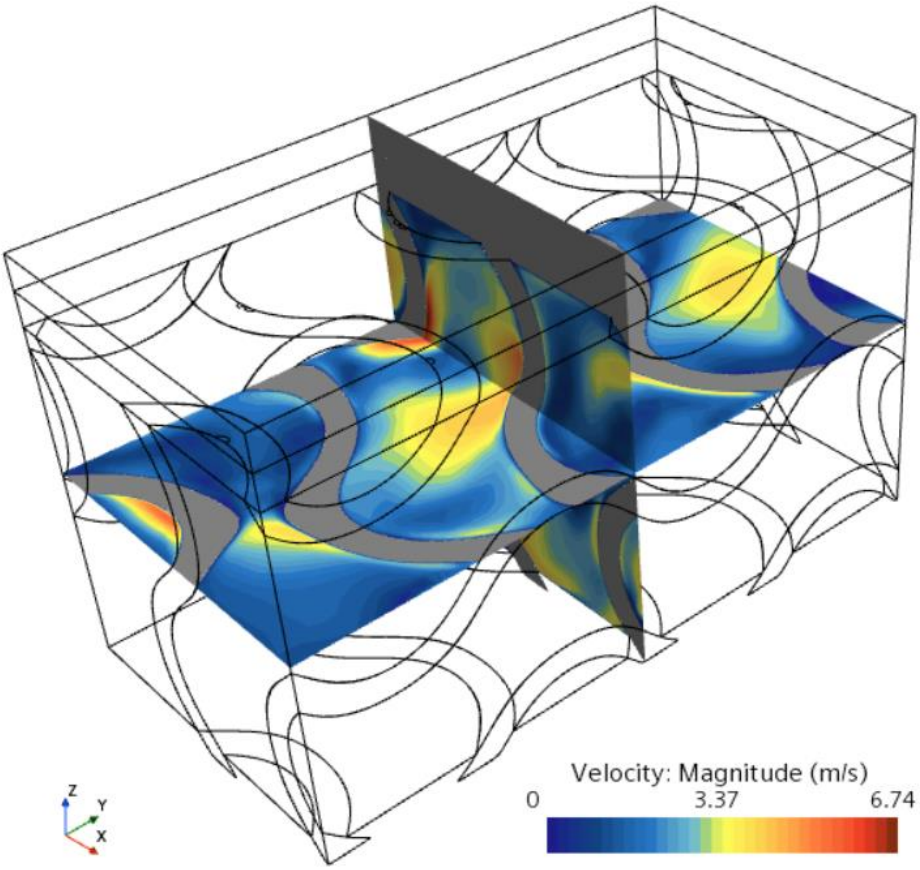

Figure 28: Velocity scene of a Gyroid with 1.2 mm wall thickness in a 10mm x 20mm x 10 mm domain

In Figure 28 is shown the velocity scene of a *Gyroid* with $1.2\,mm$ wall thickness in a $10\,mm \times 20\,mm \times 10\,mm$ domain. The velocity of water near the upper wall is very low, so it is expected to have reduced heat removal performances.

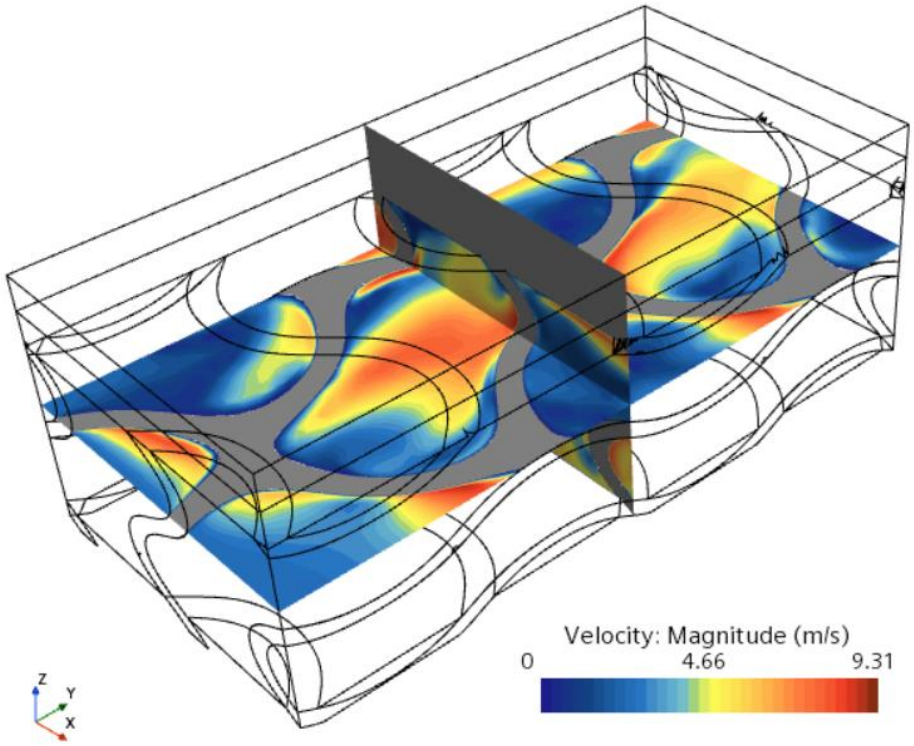

Figure 29: Velocity scene of a Gyroid with 0.8 mm wall thickness in a 10 mm x 20 mm x 5 mm domain

In Figure 29 is shown the velocity scene of a *Gyroid* with $0.8\,mm$ wall thickness in a $10\,mm \times 20\,mm \times 5\,mm$ domain. Since the thickness of the domain has been reduced to 5mm, the velocity reaches higher values, with some peaks near the upper wall, so it is expected to have better heat removal performances than the previous case.

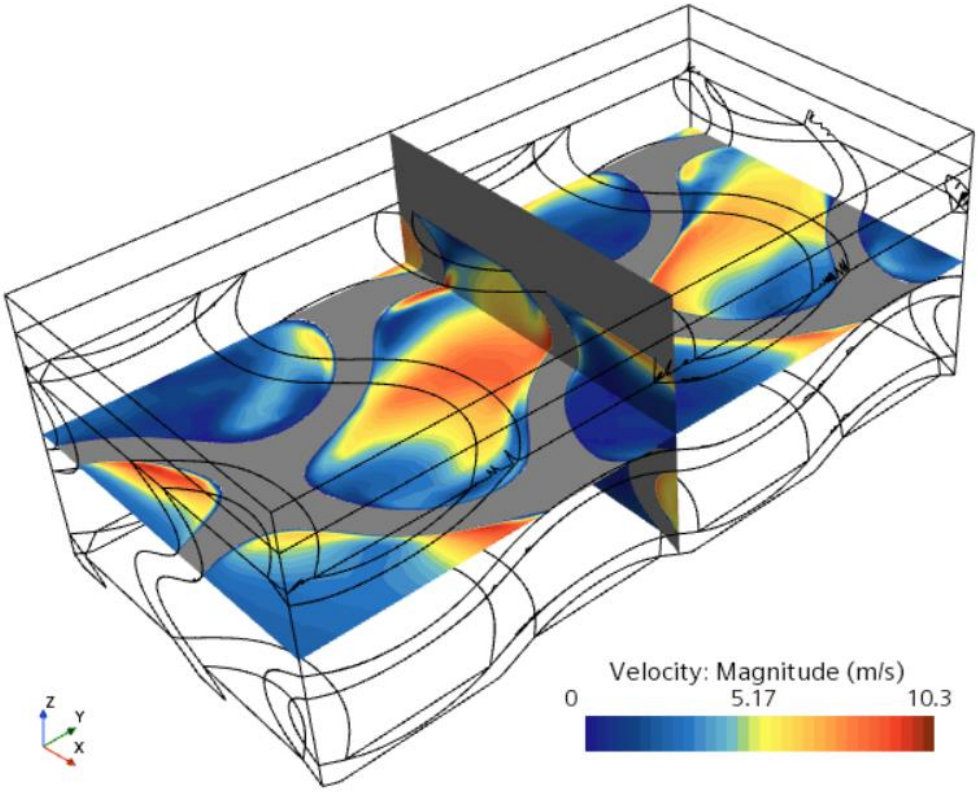

Figure 30: Velocity scene of a Gyroid with 1 mm wall thickness in a 10 mm x 20 mm x 5 mm domain

In Figure 30 is shown the velocity scene of a *Gyroid* with $0.8\,mm$ wall thickness in a $10\,mm \times 20\,mm \times 5\,mm$ domain. Increasing the wall thickness the velocity reaches higher values.

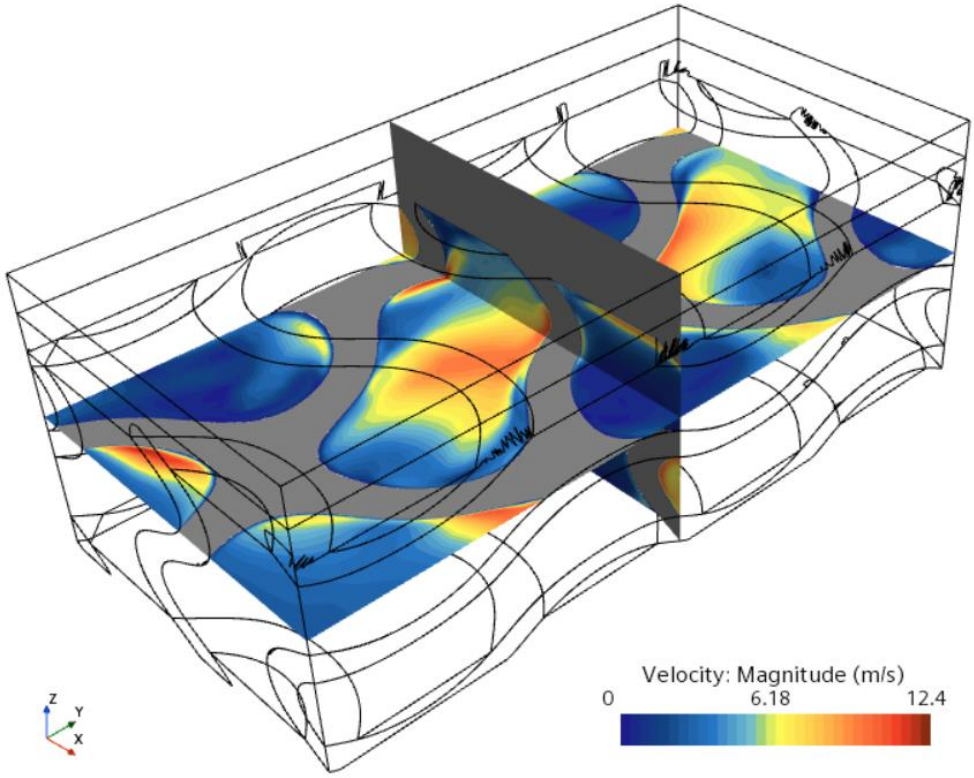

Figure 31: Velocity scene of a Gyroid with 0.8 mm wall thickness in a 10 mm x 20 mm x 5 mm domain

In Figure 31 is shown the velocity scene of a *Gyroid* with $1.2\,mm$ wall thickness in a $10\,mm \times 20\,mm \times 5\,mm$ domain. This configuration is the one with the higher values of velocity among the configuration with $Gyroid$.

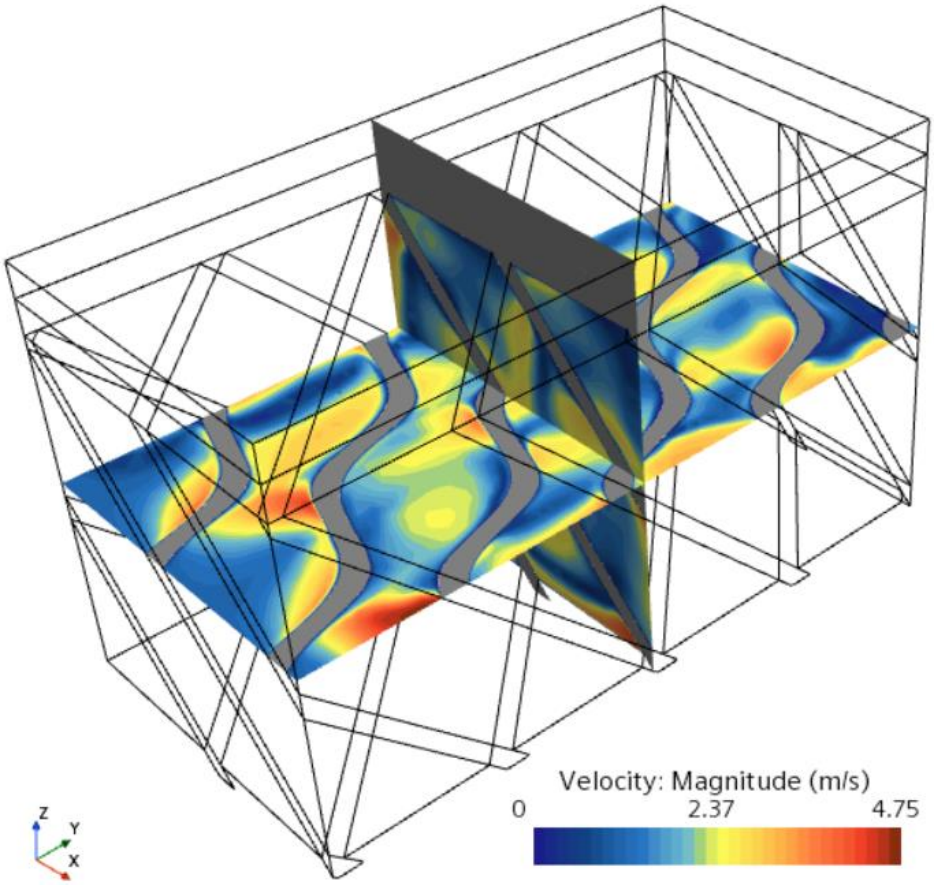

Figure 32: Velocity scene of a Diamond with 0.8 mm wall thickness in a 10 mm x 20 mm x 10 mm domain

In Figure 32 is shown the velocity scene of a *Diamond* with $0.8\,mm$ wall thickness in a $10\,mm \times 20\,mm \times 10\,mm$ domain. The velocity of water near the upper wall is very low, so it is expected to have reduced heat removal performances.

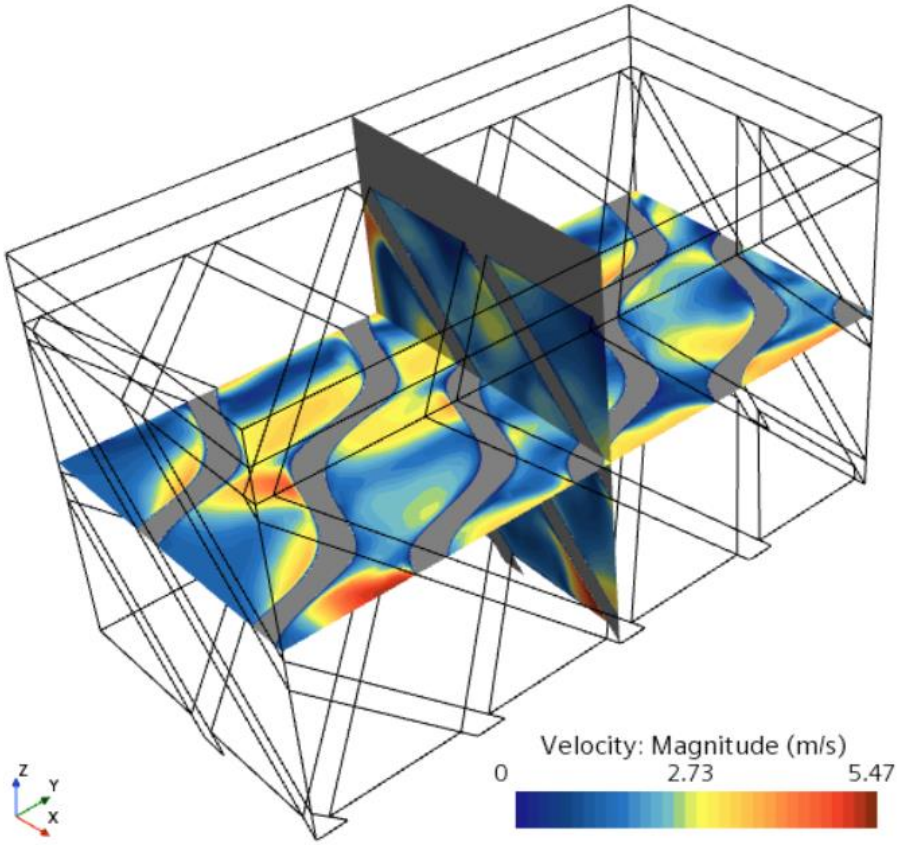

Figure 33: Velocity scene of a Diamond with 1 mm wall thickness in a 10mm x 20mm x 10 mm domain

In Figure 33 is shown the velocity scene of a *Diamond* with $1\,mm$ wall thickness in a $10\,mm \times 20\,mm \times 10\,mm$ domain. The velocity of water near the upper wall is very low, so it is expected to have reduced heat removal performances. The maximum value of velocity is like the one of $Gyroid$ in the same domain.

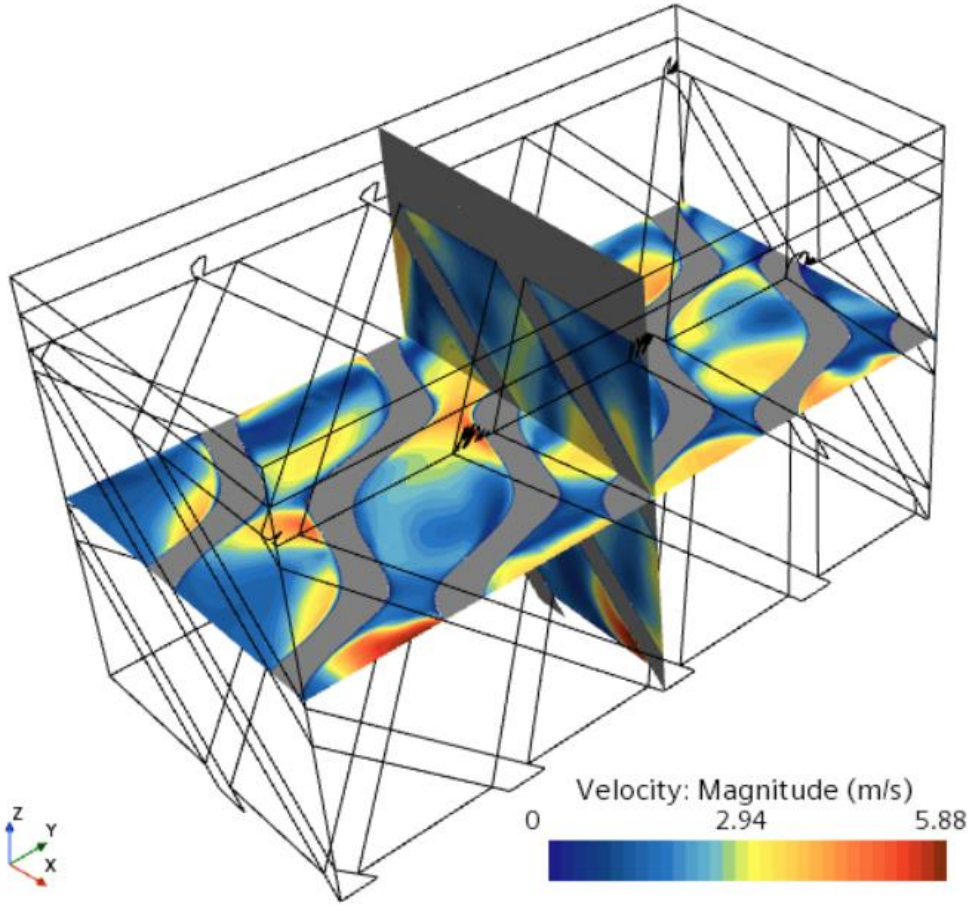

Figure 34: Velocity scene of a Diamond with 1.2 mm wall thickness in a 10mm x 20mm x 10 mm domain

In Figure 34 is shown the velocity scene of a *Diamond* with $1.2\,mm$ wall thickness in a $10\,mm \times 20\,mm \times 10\,mm$ domain. The velocity of water near the upper wall is very low, so it is expected to have reduced heat removal performances. The maximum value of velocity is like the one of $Gyroid$ in the same domain.

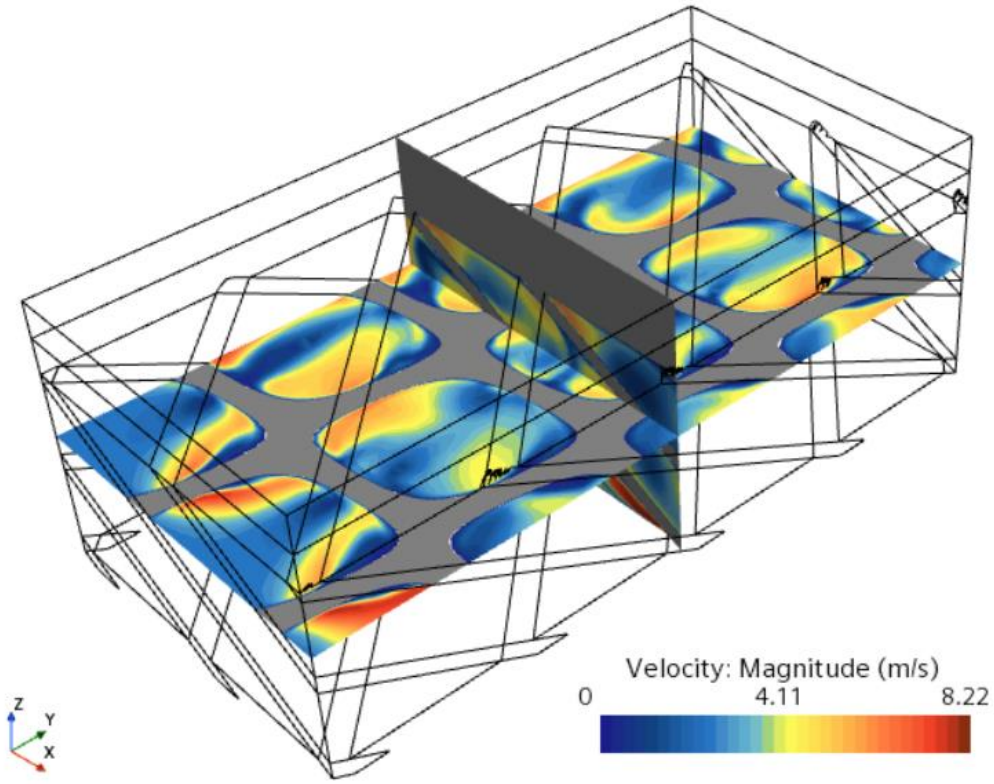

Figure 35: Velocity scene of a Diamond with 0.8 mm wall thickness in a 10 mm x 20 mm x 5 mm domain

In Figure 35 is shown the velocity scene of a *Diamond* with $0.8\,mm$ wall thickness in a $10\,mm \times 20\,mm \times 5\,mm$ domain. This configuration has lower values of velocity with respect the Gyroid in the same domain, but the peaks of velocity are closer to the upper wall, so better thermal capabilities are expected.

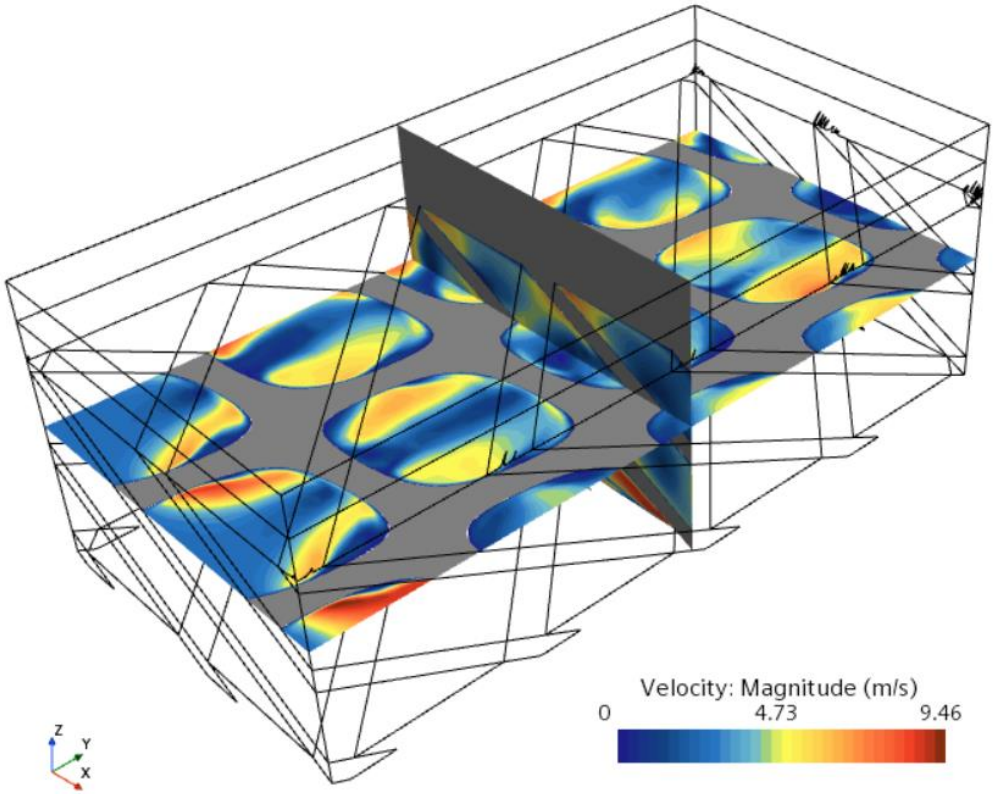

Figure 36: Velocity scene of a Diamond with 1 mm wall thickness in a 10 mm x 20 mm x 5 mm domain

In Figure 36 is shown the velocity scene of a *Diamond* with $1\,mm$ wall thickness in a $10\,mm \times 20\,mm \times 5\,mm$ domain.

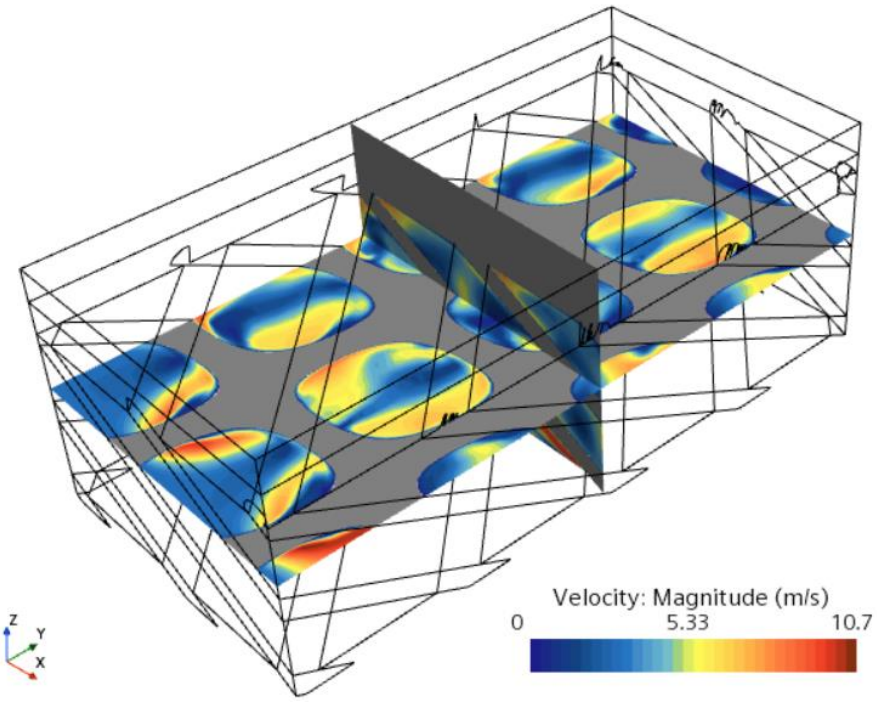

Figure 37: Velocity scene of a Diamond with 1.2 mm wall thickness in a 10 mm x 20 mm x 5 mm domain

In Figure 37 is shown the velocity scene of a *Diamond* with $1.2\,mm$ wall thickness in a $10\,mm \times 20\,mm \times 5\,mm$ domain. This configuration has lower values of velocity with respect the Gyroid in the same domain, but the peaks of velocity are closer to the upper wall, so better thermal capabilities are expected. Since this configuration has the bigger values of velocity among the configurations with *Diamond*, it will probably have the best thermal performances overall.

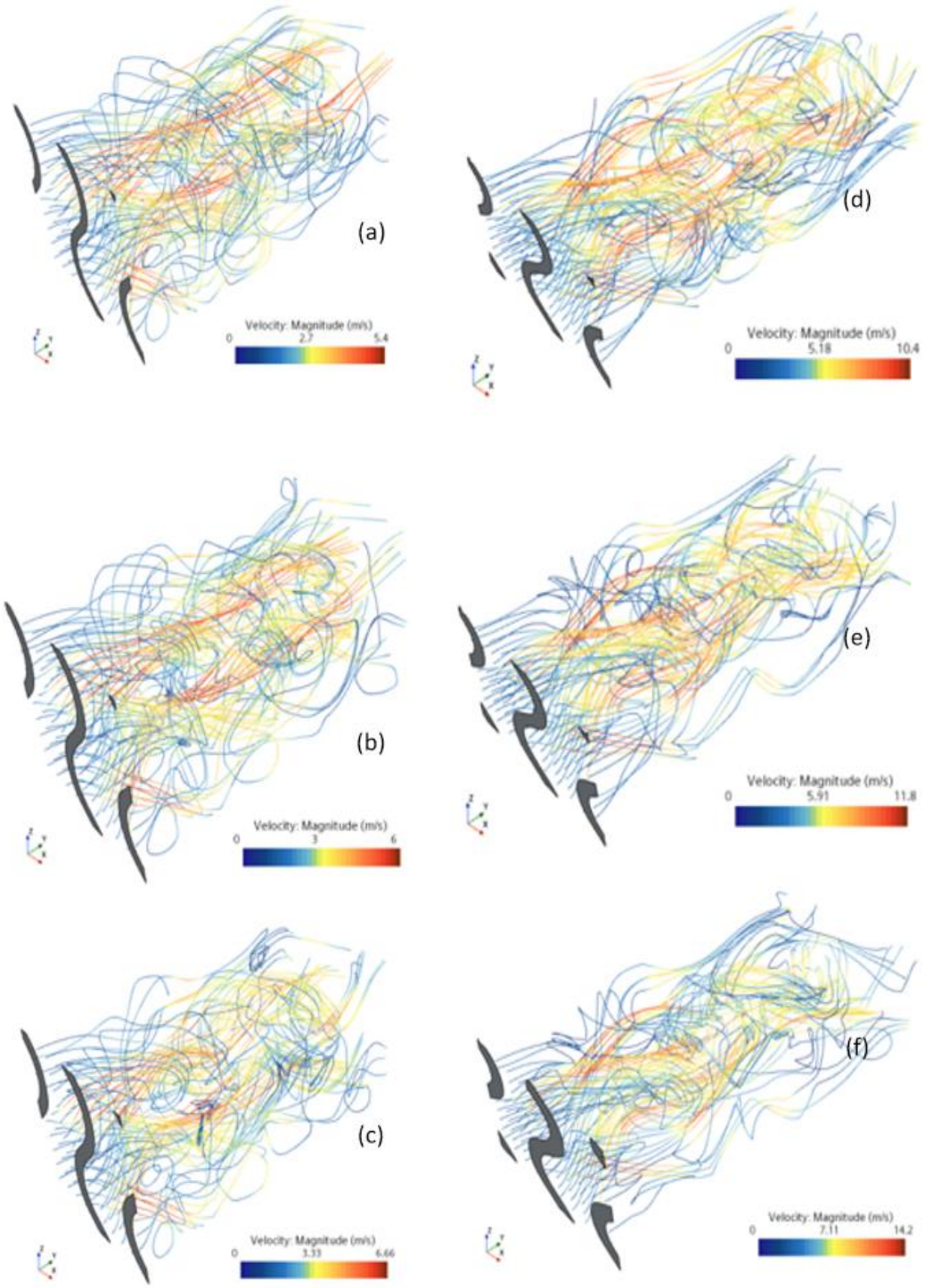

Figure 38: velocity magnitude streamlines of the Gyroid in two domains. Wall thickness: (a) 0.8 mm (b) 1 mm (c) 1.2 mm (d) 0.8 mm e) 1 mm (f) 1.2 mm

In Figure 38 are shown the velocity streamlines for every $Gyroid$ combinations. The streamlines cover uniformly every part of the domain.

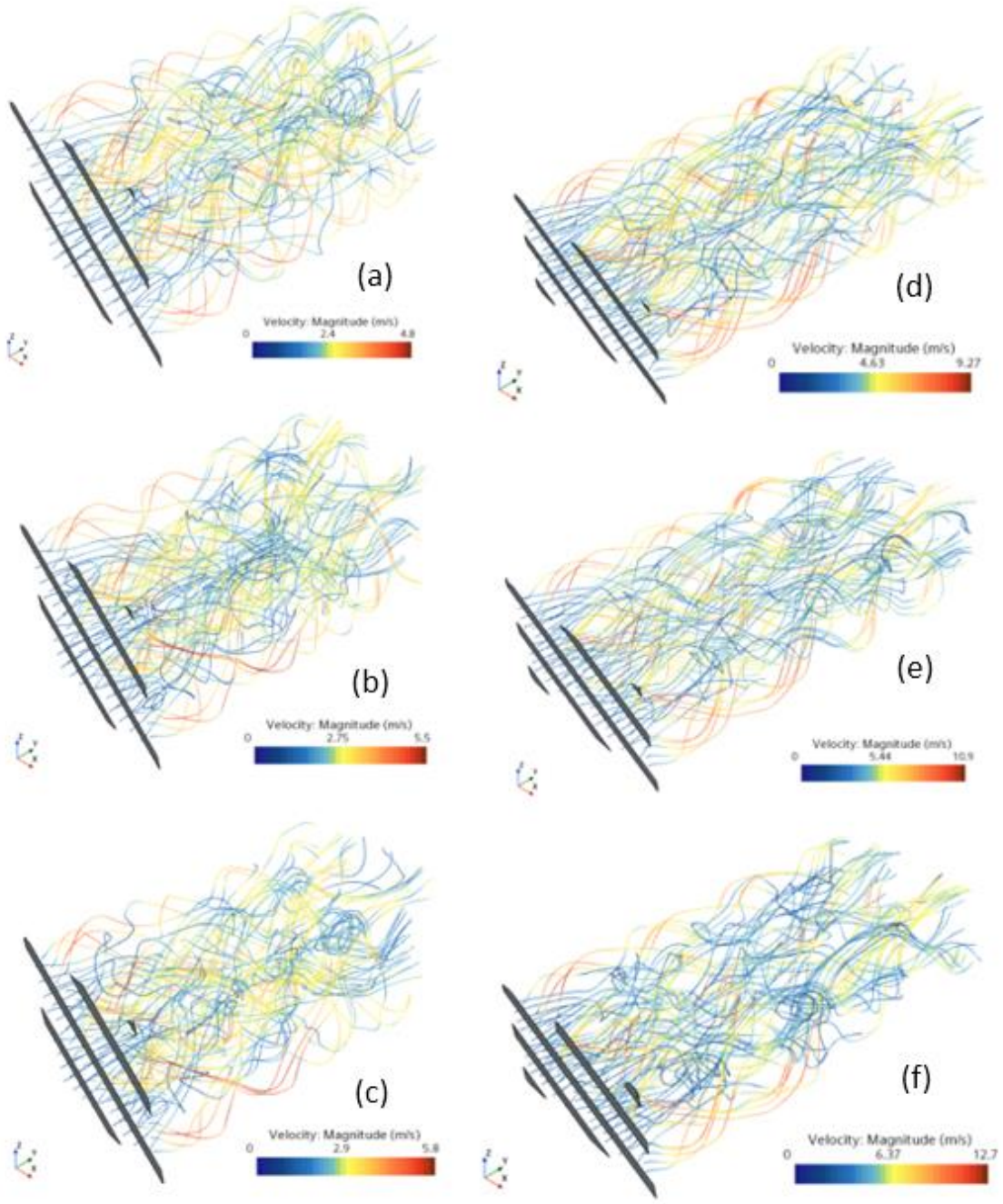

Figure 39: velocity magnitude streamlines of the Diamond in two domains. Wall thickness: (a) 0.8 mm (b) 1 mm (c) 1.2 mm (d) 0.8 mm e) 1 mm (f) 1.2 mm

In Figure 39 are shown the velocity streamlines for every $Diamond$ combinations. The streamlines cover uniformly every part of the domain.

Thermal results

In this section are shown the thermal results of the small domains.

The magnitude of the heat flux is increased until reaches the limits for boiling. Every solid material respects the constraints on the temperature, so the bottle neck is the water temperature.

The value of the heat flux is chosen to avoid boiling of the water, it is increased until the boiling condition reaches the limit. Infact, to check the presence of boiling, the difference between the local temperature of the water and the saturation temperature at the respective local pressure must be positive.

$$Boiling \ \ if \ \ T - T_{sat} > 0$$

The temperature of the solid part (on the left) and of the fluid (on the right) are displayed separately from Figure 40 to Figure 43. The applied heat flux is listed in the table linked to the figure.

$Configuration$	$Wall\ thickness\ [mm]$	$Pressure\ drop\ [bar]$	$Heat\ flux\ [\frac{MW}{m^2}]$
a	0.80	0.10±0.0010	4.2
b	1.00	0.13±0.0012	4.95
c	1.20	0.15±0.0014	5.2

Table 14: wall thickness, pressure drop, heat flux of the Gyroid in a 10mm x 20mm x 10 mm domain

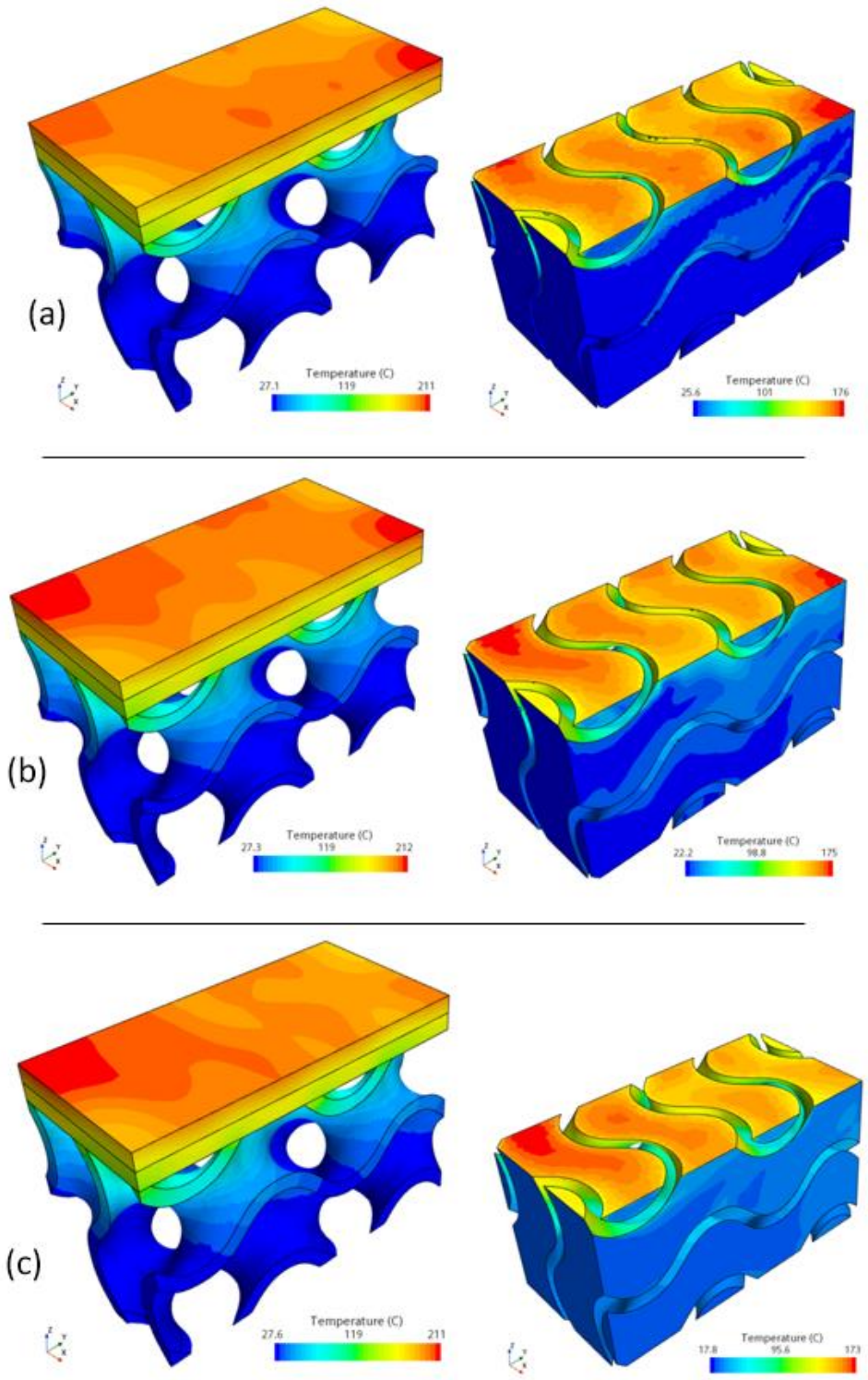

Figure 40: Gyroid with 0.8 mm (a), 1 mm (b), 1.2 mm (c) wall thickness

The maximum value of the heat flux is quite the same in all the three configurations (**Error! Reference source not found.**), in fact they have almost the same pressure drop in the range $0.1\ bar \div 0.15\ bar$.

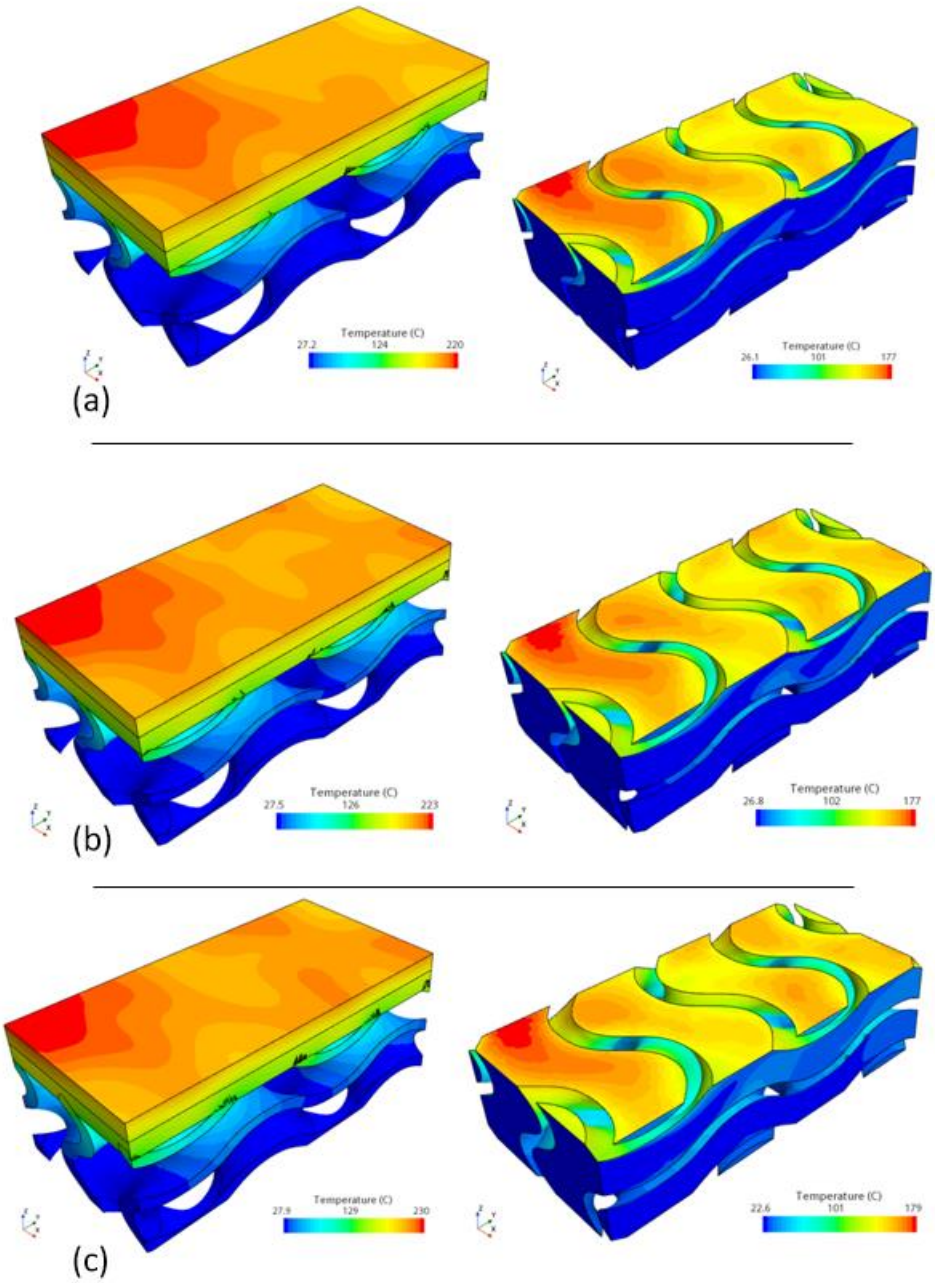

Figure 41: Gyroid with 0.8 mm (a), 1 mm (b), 1.2 mm (c) wall thickness

Looking to Figure 41, configuration $'c'$ can sustain the highest value of heat flux, this is due to the bigger pressure drop (Table 15).

$Configuration$	$Wall\ thickness\ [mm]$	$Pressure\ drop\ [bar]$	$Heat\ flux\ [\frac{MW}{m^2}]$
a	0.80	0.33±0.003	5.95
b	1.00	0.40±0.004	6.20
c	1.20	0.55±0.005	7.00

Table 15: wall thickness, pressure drop, heat flux of the Gyroid in a 10mm x 20mm x 5 mm domain

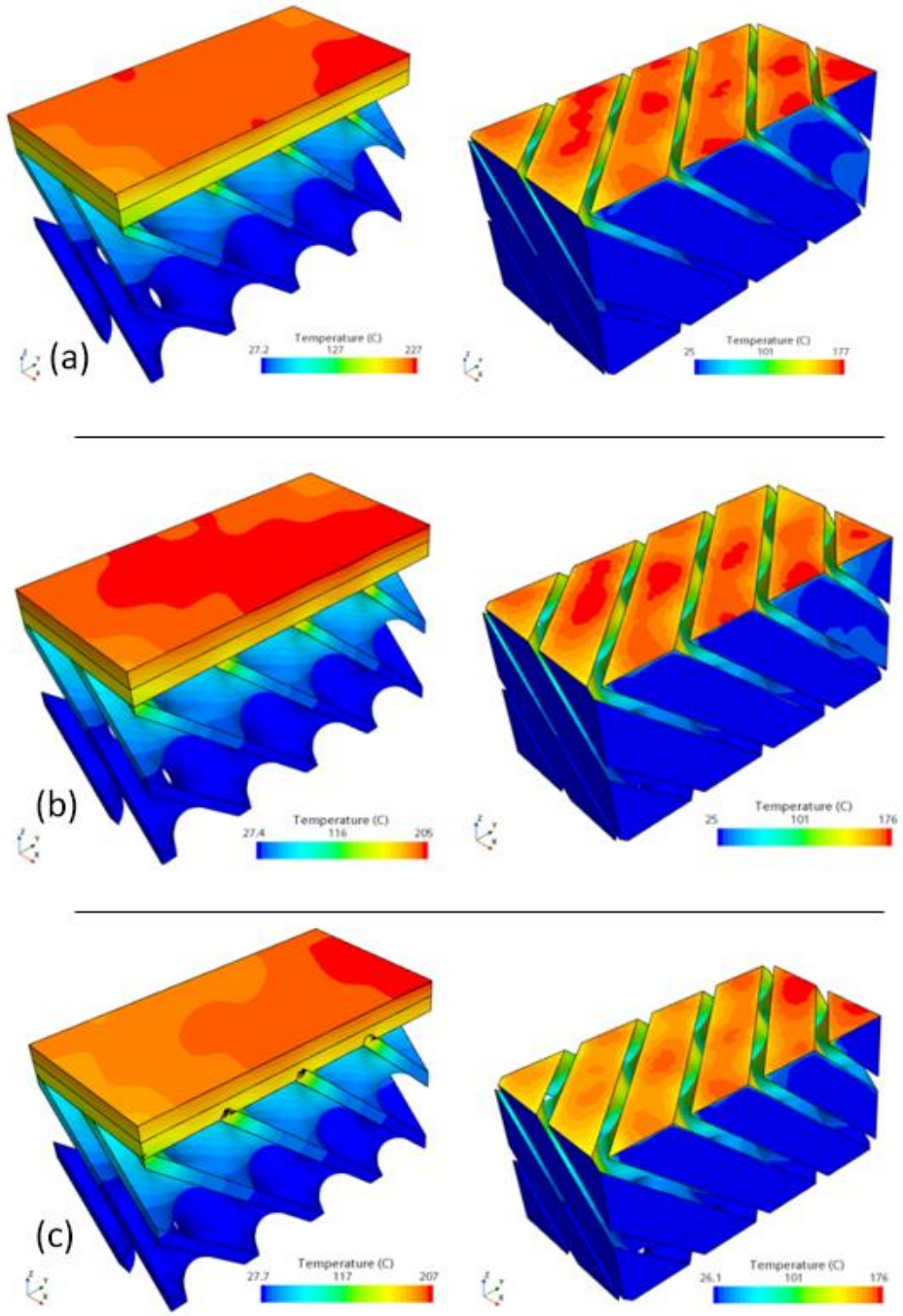

Figure 42: Diamond with 0.8 mm (a), 1 mm (b), 1.2 mm (c) wall thickness

Configuration $'c'$ can sustain higher heat flux, without boiling, due to its slightly increased pressure drop. (Table 16)

$Configuration$	$Wall\ thickness\ [mm]$	$Pressure\ drop\ [bar]$	$Heat\ flux\ [\frac{MW}{m^2}]$
a	0.80	0.10±0.0010	5.8
b	1.00	0.13±0.0012	6.0
c	1.20	0.15±0.0014	6.8

Table 16: wall thickness, pressure drop, heat flux of the Diamond in a 10mm x 20mm x 10 mm domain

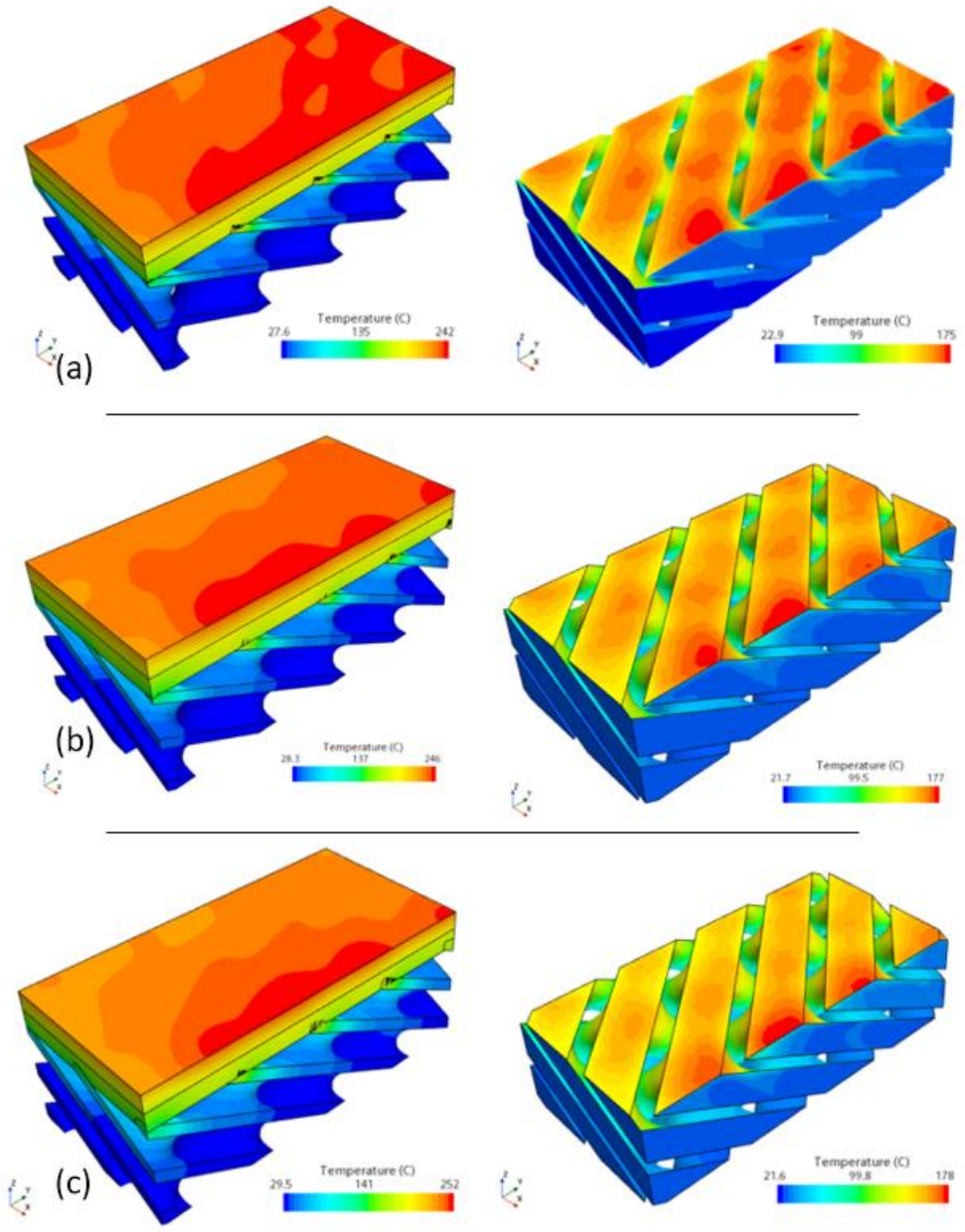

Figure 43: Diamond with 0.8 mm (a), 1 mm (b), 1.2 mm (c) wall thickness

Configuration $'c'$ reaches the highest value of heat flux overall. But its pressure drop is identic to the Gyroid in the same domain, so the improved performances are also due to geometry effects.

$Configuration$	$Wall\ thickness\ [mm]$	$Pressure\ drop\ [bar]$	$Heat\ flux\ [\frac{MW}{m^2}]$
a	0.80	0.30±0.0028	8.0
b	1.00	0.41±0.0038	9.4
c	1.20	0.55±0.0051	10.0

Table 17: wall thickness, pressure drop, heat flux of the Diamond in a 10mm x 20mm x 5 mm domain

To find correlations between the maximum value of heat flux and the TPMS configuration, it is plotted as a function of the $\frac{surface}{volume_{solid}}$ in Figure 44.

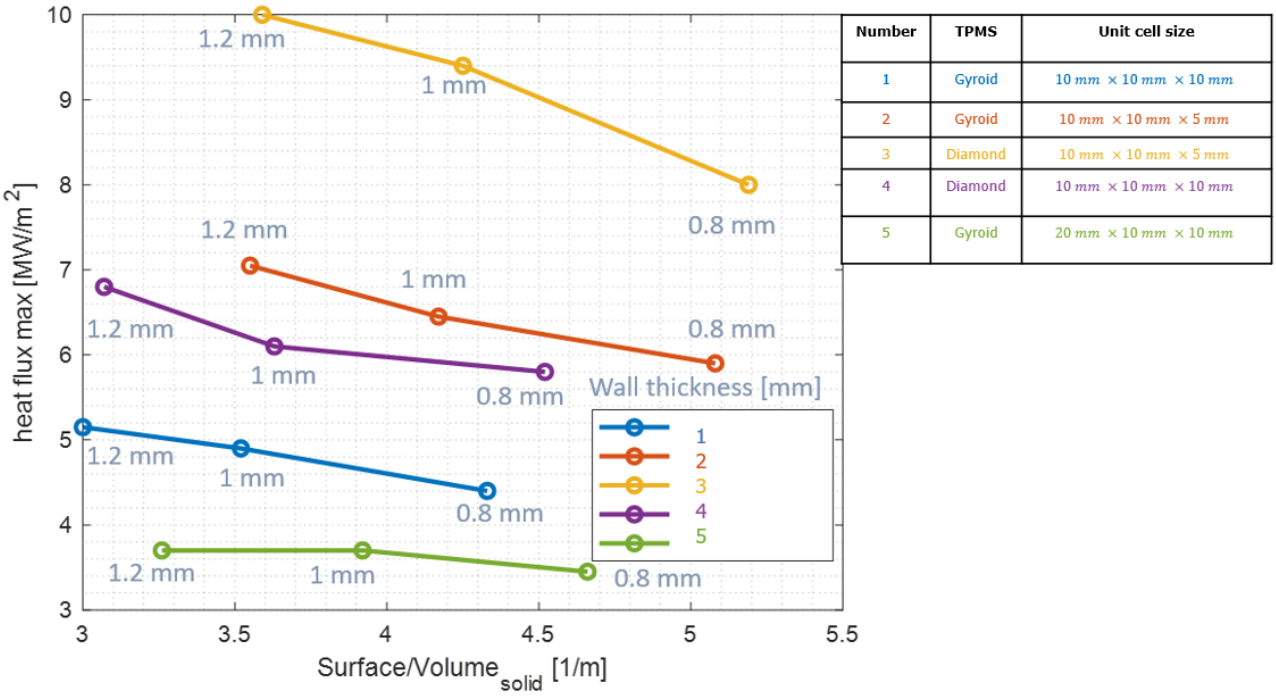

Number	TPMS	Unit cell size
1	Gyroid	$10\ mm \times 10\ mm \times 10\ mm$
2	Gyroid	$10\ mm \times 10\ mm \times 5\ mm$
3	Diamond	$10\ mm \times 10\ mm \times 5\ mm$
4	Diamond	$10\ mm \times 10\ mm \times 10\ mm$
5	Gyroid	$20\ mm \times 10\ mm \times 10\ mm$

Figure 44: maximum heat flux as a function of the $\frac{surface}{volume_{solid}}$

The diamond with a unit cell size of $10\ mm \times 10\ mm \times 5\ mm$ reaches the highest heat flux, and the configurations with the lower value of the wall thickness seem to have better cooling capabilities, but has not been identified any other appreciable trend.

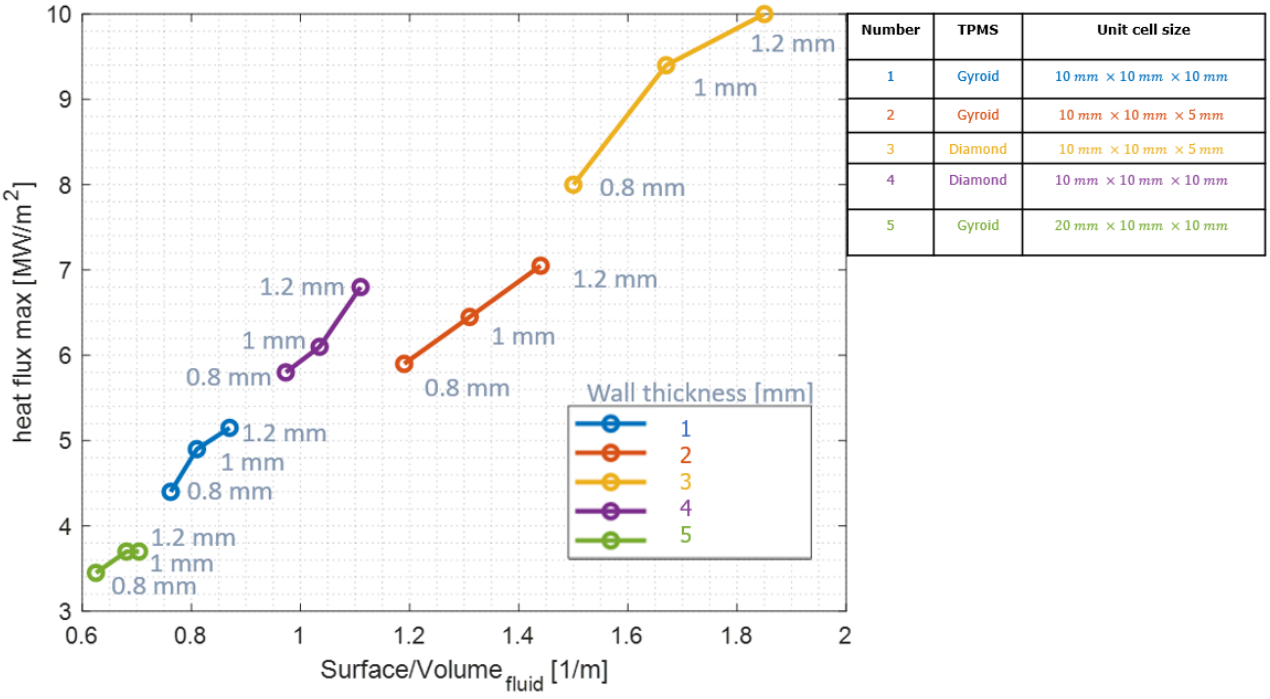

Number	TPMS	Unit cell size
1	Gyroid	$10\,mm \times 10\,mm \times 10\,mm$
2	Gyroid	$10\,mm \times 10\,mm \times 5\,mm$
3	Diamond	$10\,mm \times 10\,mm \times 5\,mm$
4	Diamond	$10\,mm \times 10\,mm \times 10\,mm$
5	Gyroid	$20\,mm \times 10\,mm \times 10\,mm$

Figure 45: Maximum heat flux as a function of the $\frac{surface}{volume_{fluid}}$

In Figure 45 the heat flux is plotted as a function of the $\frac{surface}{volume_{fluid}}$. Now a linear relation is appreciable, and the Diamond with unit cell size $10mm \times 10mm \times 5mm$ is again thermically the best. Could be interesting to analyze other configurations with also other TPMS to see if this linear trend is valid again. With these results is clear that the unit cell sizes of $10mm \times 10mm \times 5mm$ have the best performances, because they can guarantee higher pressure drops given the same mass flow rate. Is known that the higher is the pressure drop the more is the thermal exchange. But the pressure drop is not the only parameter that determines the best configuration. Infact, given a unit cell size, the Diamond and the Gyroid share the same value of pressure drop, but looking to the results Diamond has better performances. This means that other dependences must be found: one could be the porosity, as well as the Reynolds and Nusselt Number.

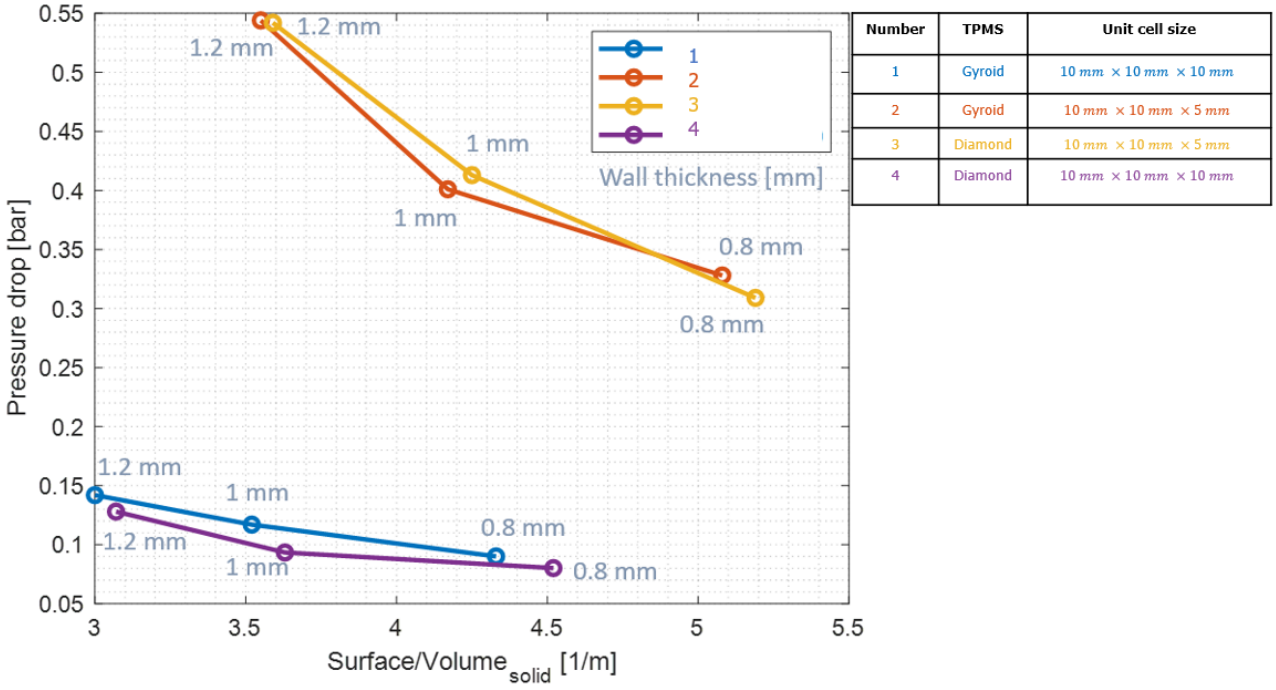

Number	TPMS	Unit cell size
1	Gyroid	$10\ mm \times 10\ mm \times 10\ mm$
2	Gyroid	$10\ mm \times 10\ mm \times 5\ mm$
3	Diamond	$10\ mm \times 10\ mm \times 5\ mm$
4	Diamond	$10\ mm \times 10\ mm \times 10\ mm$

Figure 46: Pressure drop as a function of the $\frac{surface}{volume_{solid}}$

The $pressure\ drop\ [bar]$ is plotted as a function of the $\frac{surface}{volume_{solid}}$. As expected, the configurations with a unit cell size of $10\ mm\ \times 10\ mm\ \times 5\ mm$ that have the bigger pressure drop, are also the one that can guarantee the best thermal performances.

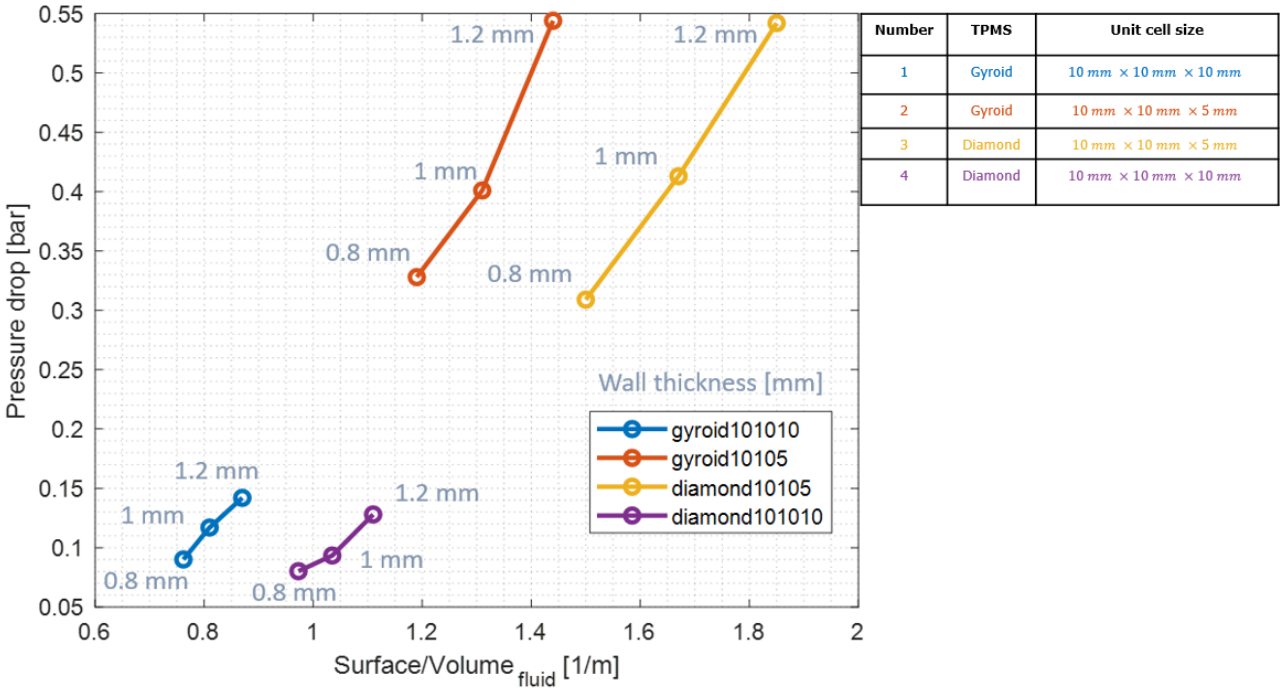

Number	TPMS	Unit cell size
1	Gyroid	$10\ mm \times 10\ mm \times 10\ mm$
2	Gyroid	$10\ mm \times 10\ mm \times 5\ mm$
3	Diamond	$10\ mm \times 10\ mm \times 5\ mm$
4	Diamond	$10\ mm \times 10\ mm \times 10\ mm$

Figure 47: Pressure drop as a function of the $\frac{surface}{volume_{fluid}}$

Given a TPMS, there is a linear relation of the $pressure\ drop\ [bar]$ as a function of the $\frac{surface}{volume_{fluid}}$.

As a result, the more promittent configurations have a unit cell size of $10\ mm\ \times 10\ mm\ \times 5\ mm$. Among them, the Diamond seems to be the best, so it will be used in the tile configuration described in the next Chapter.

Chapter 4: Model for the entire tile

4.1 Tile configuration and boundary conditions

The divertor units will be composed of modules connected in parallel. Every module is made of 8 identic tiles connected in parallel as shown in Figure 48. Due to the constraints related to the available pumps, the maximum mass flow rate available for a module is $1{,}25\ \frac{kg}{s}$ with a maximum pressure drop of $15\ bar$.

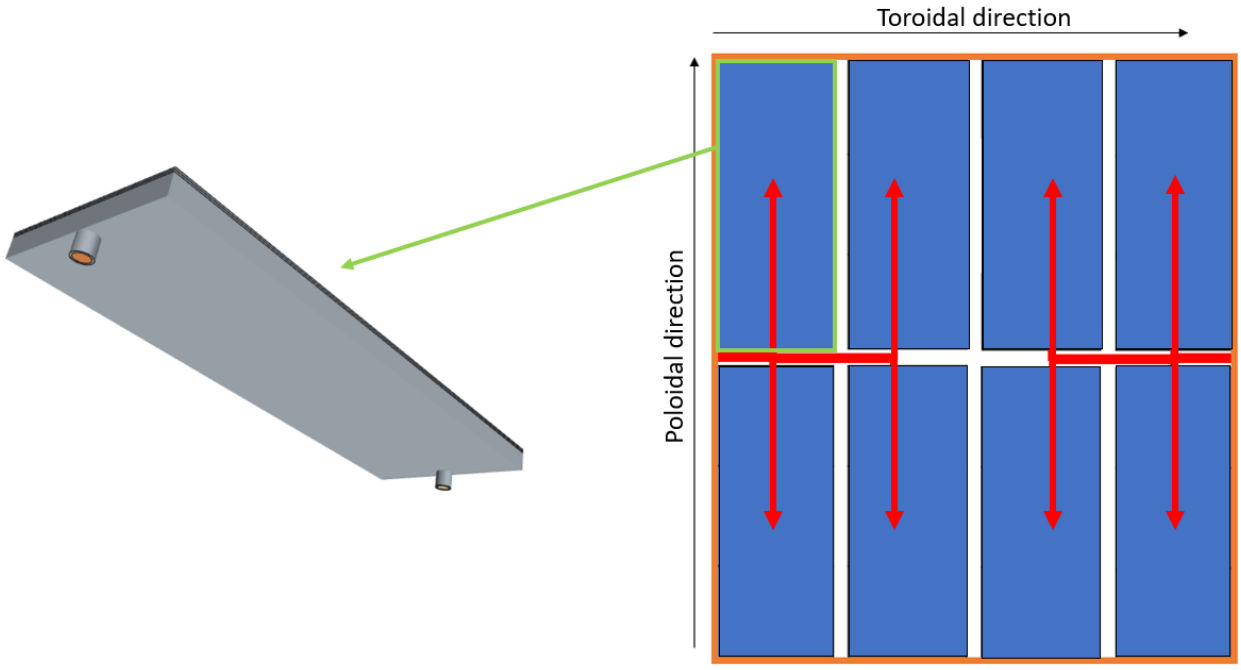

Figure 48: Target module

Once the best combination of TPMS and domain thickness is identified, it can be inserted into the tile design. As derived in the previous section, the most promising combination is the Schwarz Diamond in a $5\ mm$ thickness domain. The Diamond unit cell size, the porosity and the wall thickness used are reported in the following table.

$Wall\ thickness\ [mm]$	$Unit\ cell\ size\ [mm^3]$	$Porosity\ [\%]$
1,2	$10\ mm\ \times\ 10\ mm\ \times\ 5\ mm$	52,82

Table 18: unit cell size porosity and wall thickness of the Schwarz Diamond used inside the Tile

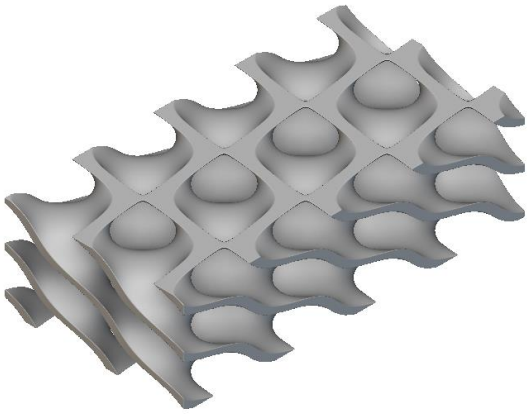

Figure 49: TPMS chosen to be used in the final tile design

The tile dimensions are $302\ mm\ \times 102\ mm\ \times 8\ mm$ (look to the drafting in the next page).

The TPMS has a space of $5\ mm$ thickness available. A back plate of CuCrZr contains the TPMS structure made of the same material. On the top, a $1\ mm$ Tungsten lid covers the entire tile so that it will be the plasma facing part. A Soft Copper $1\ mm$ layer is inserted between the Tungsten lid and the TPMS lattice to avoid excessive mismatch due to thermal expansion. The inlet and outlet are composed by two $8\ mm$ internal radius pipes, they will be welded to the manifolds. The drafting of the entire tile and its expanded view are shown in the next pages.

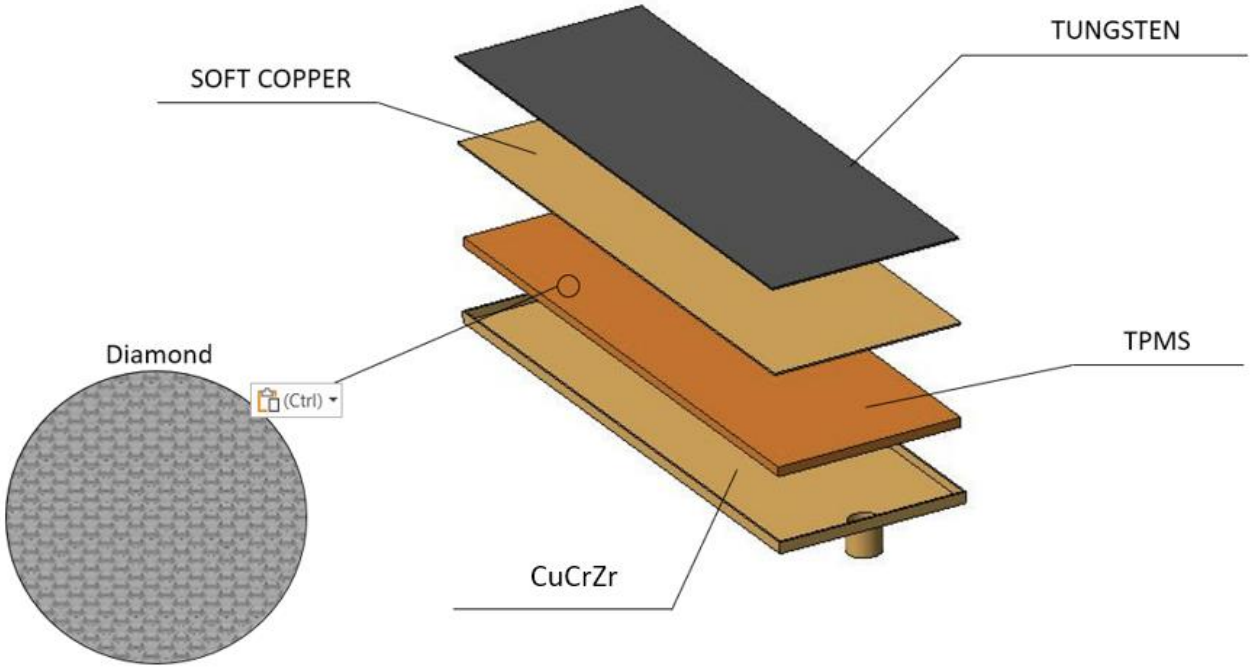

Figure 50: exploded view of the tile

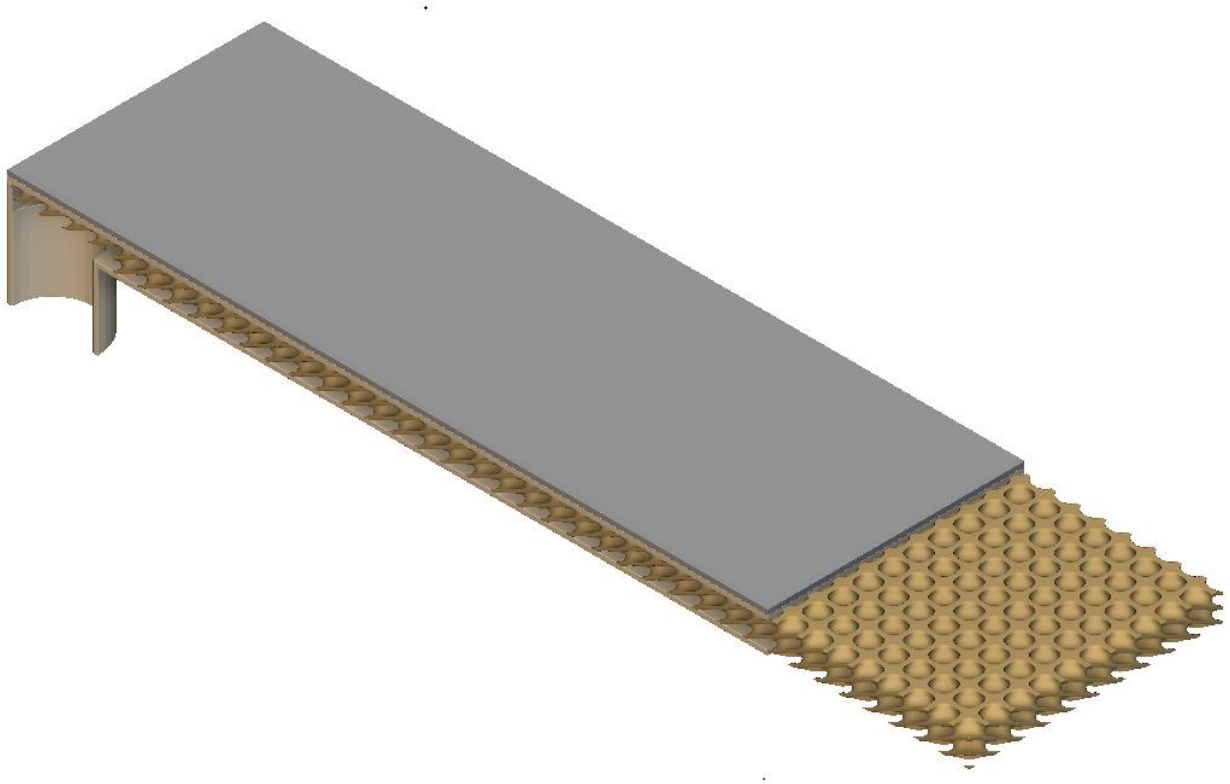

Figure 51: View of a quarter of the tile

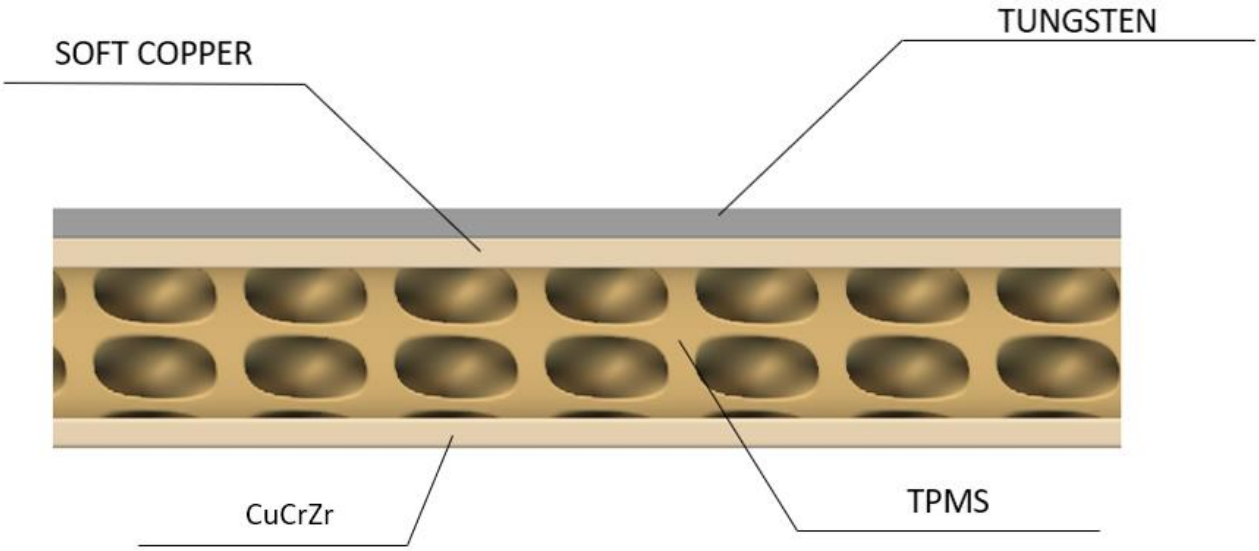

Figure 52: Layers inside the tile

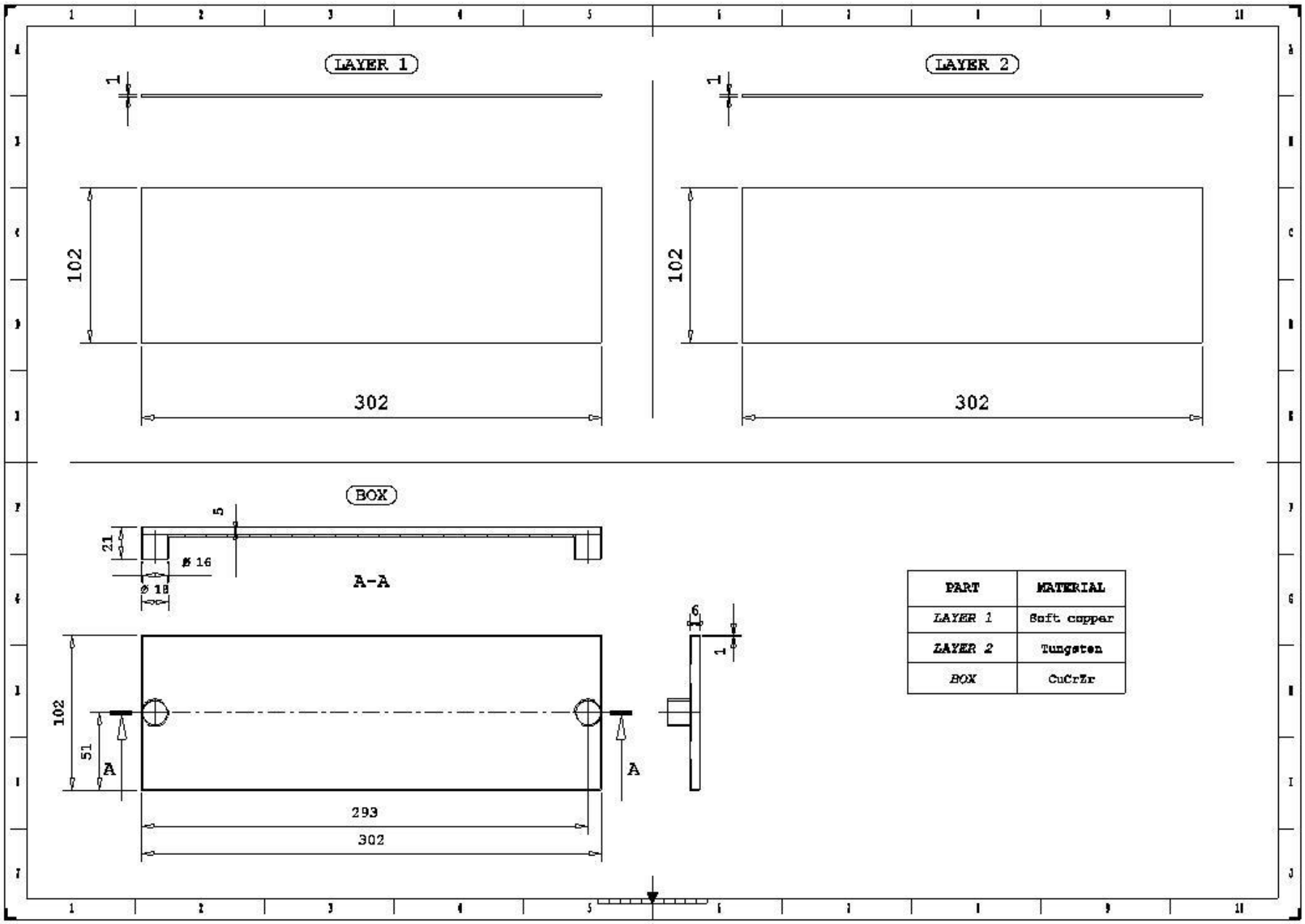

PART	MATERIAL
LAYER 1	Soft copper
LAYER 2	Tungsten
BOX	CuCrZr

4.2 Boundary conditions

There are some limits regarding the supply of water: pumps are very expensive, and the construction of a new water circuit would increase the costs of the project. Today there is only one pump that can supply $5\frac{kg}{s}$ of water. Our design is based on the hypothesis that another identic pump will be bought. Thus considering $10\frac{kg}{s}$ of available mass flow rate for a module, every tile has $1{,}25\frac{kg}{s}$ imposed at the inlet, while a pressure of $10\ bar$ at the outlet with roughly maximum 15 bar pressure drop per module.

4.3 Material properties

All the properties have been considered independent from the temperature.

Property	Value
$Density\ [\frac{kg}{m^3}]$	8800
$Specific\ heat\ [\frac{J}{kg \cdot K}]$	410
$Thermal\ conductivity\ [\frac{W}{m \cdot K}]$	340

Table 19: Copper properties

The fluid is common water which properties are reported in Table 20. At the inlet a mass flow rate of $1{,}25\ kg/s$ is imposed, instead, $10\ bar$ as the outlet pressure condition.

Property	Value
$Density\ [\frac{kg}{m^3}]$	997,5
$Dynamic\ Viscosity\ [Pa \cdot s]$	$8{,}887e-4$
$Specific\ heat\ [\frac{J}{kg \cdot K}]$	4181,72
$Thermal\ conductivity\ [\frac{W}{m \cdot K}]$	0,62

Table 20: Water properties

Property	Value
$Density\ [\frac{kg}{m^3}]$	19300
$Specific\ heat\ [\frac{J}{kg \cdot K}]$	134
$Thermal\ conductivity\ [\frac{W}{m \cdot K}]$	163,2

Table 21: Tungsten properties

Property	Value
$Density\ [\frac{kg}{m^3}]$	8800
$Specific\ heat\ [\frac{J}{kg \cdot K}]$	410
$Thermal\ conductivity\ [\frac{W}{m \cdot K}]$	340

Table 22: Soft Copper properties

4.4 Models and mesh

The models are the same used in the previous reduced domains simulations. The Reynolds Averaged Navier-Stokes (RANS) equations are used, the SST k −ω as closure equation and with an All y+ approach.

The mesh settings are listed in Table 23.

$Base\ size\ [mm]$	$Number\ of\ prism\ layers\ [mm]$	$Prism\ layer\ near\ wall\ thickness\ [m]$	$Prism\ layer\ total\ thickness\ [mm]$
1.5	5	5e-6	0.5

Table 23: Mesh parameters

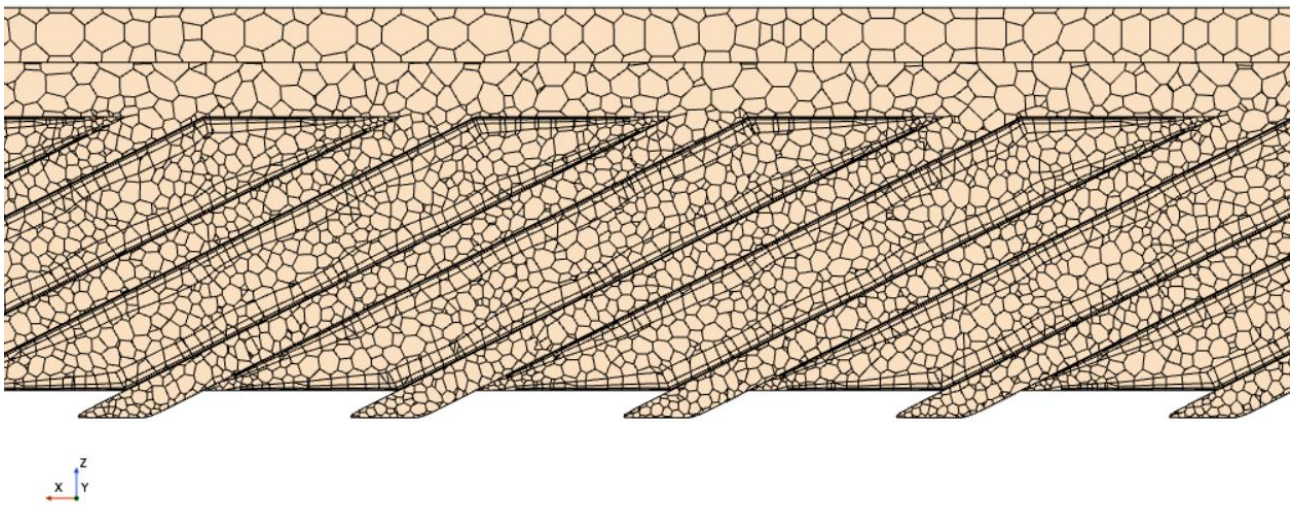

Figure 53: Tile mesh

4.5 Results

4.5.1 Hydraulic results

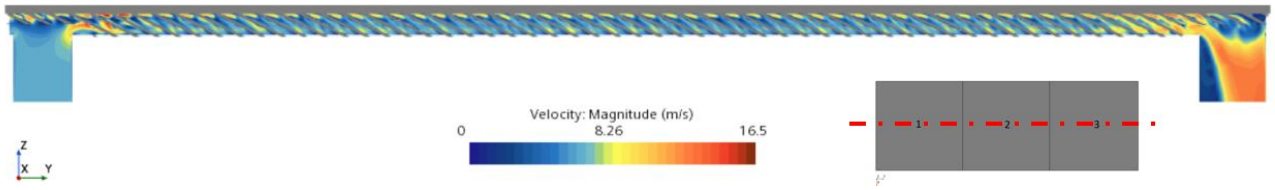

Figure 54: Velocity scene in a section along the horizontal axis of the tile.

In Figure 54 is shown the velocity in a cross section along the horizontal axis of the tile.

The thermal performances are improved by increasing the velocity, consequently, for having the best thermal removal efficiency the bigger values of velocity should be located near the upper wall of the tile. All the other peaks of velocity are useless, and they only increase the pressure drop. To see if the tile performs well in that way, the velocity scenes have been derived in four cross sections along the tile as shown in Figure 55. Cross section 1 is after the length of 2-unit cells (so after 20 mm from the inlet), and since the TPMS are periodic, after every multiple of the length of one unit cells we find the same cross section.

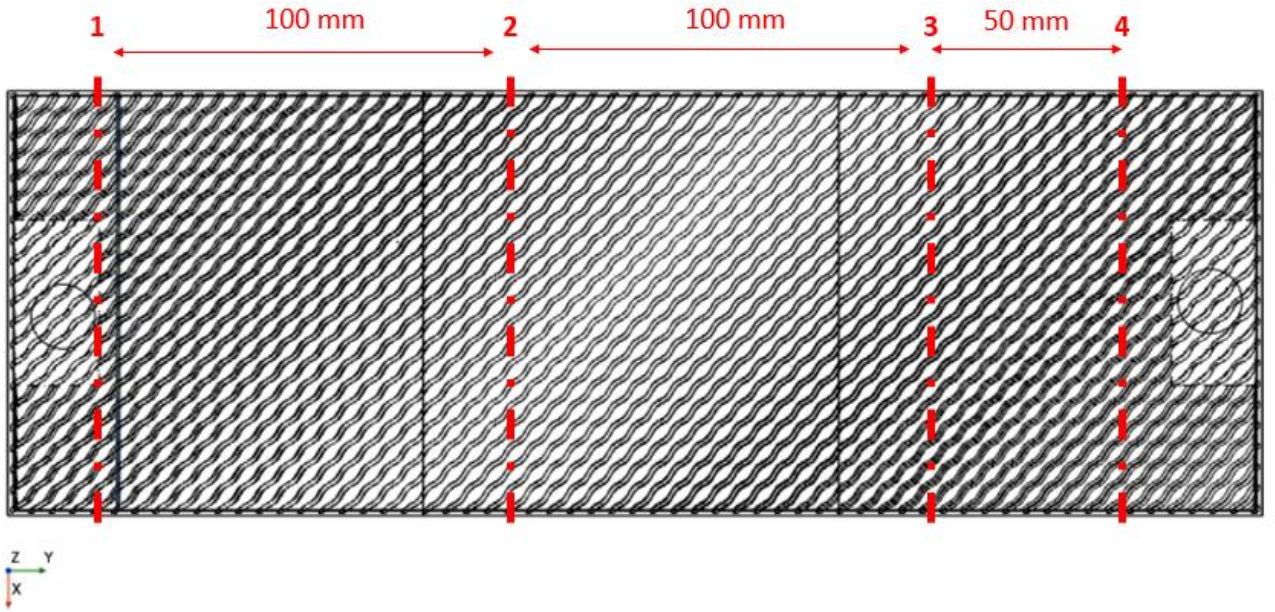

Figure 55: Cross sections

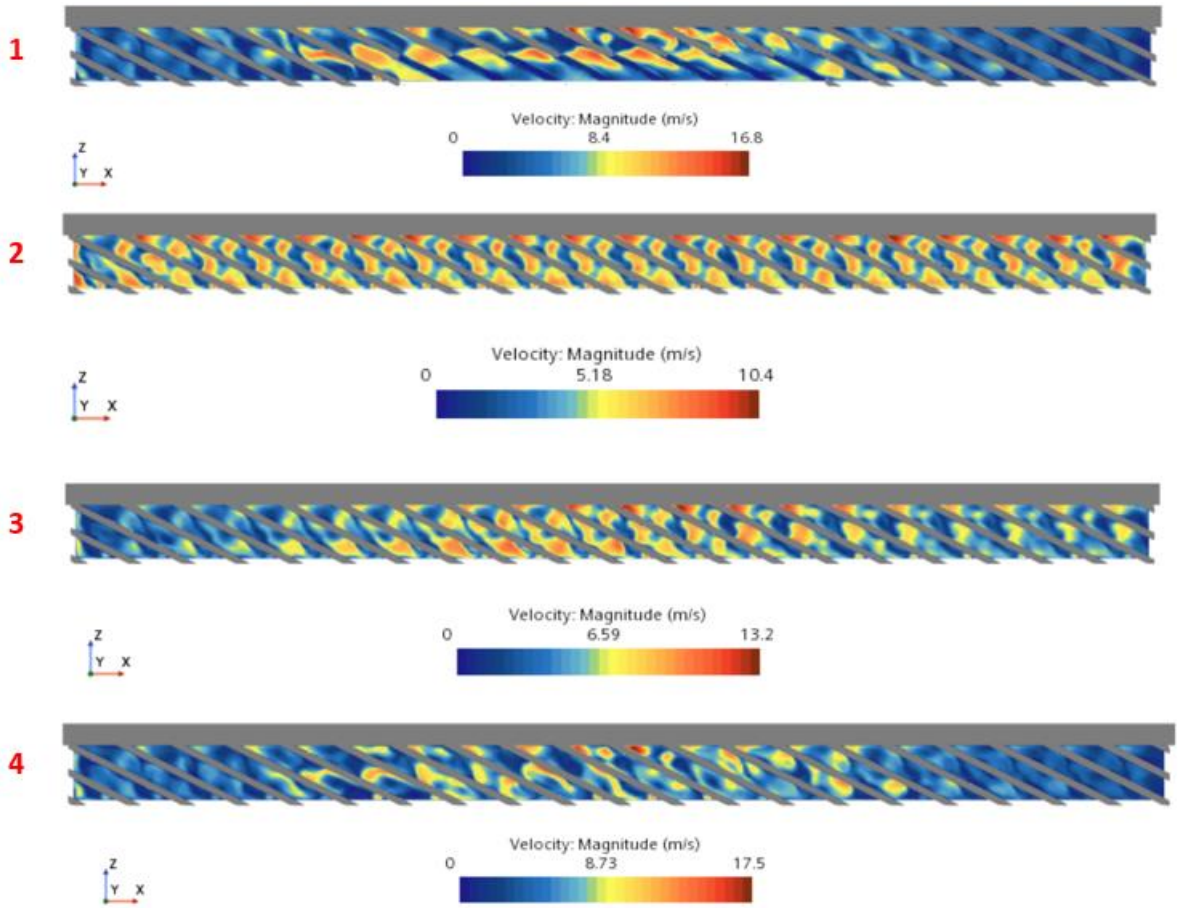

Figure 56: Velocity distribution in three cross sections, the first is near the inlet, the second in the middle and the last near the outlet.

Looking to the cross section 1, the velocity peaks are concentrated at the center of the section because the flow doesn't have the time to distribute in the tile. Instead going to cross section 2, peaks of velocity distribute in all the section, the peaks in the lower part of the tile provide useless pressure losses. Cross section 3 already feels the presence of the outlet, that attracts the flow from the sides of the tile. In fact, the velocity peaks go back to the center of the section, so that the sides of the tile are less cooled, that is why the regions near the outlet are the worst for boiling. Further improvements on the design could improve this behavior.

The pressure is well distributed between inlet and outlet, the pressure drop is equal to $11\ bar$, that is below the limit of $15\ bar$.

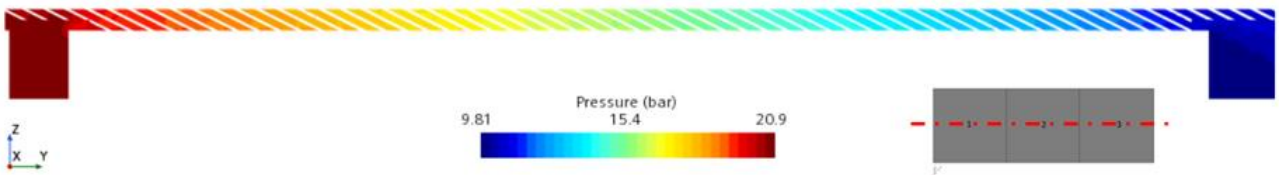

Figure 57: Pressure in a section along the horizontal axis of the tile.

4.5.2 Thermal results

The way the heat flux hits the target depends on the magnetic configuration. Since different magnetic configurations will be expected, the tile must guarantee to exhaust the incoming power for every configuration, also in accident conditions. For this reason, the entire tile is equipped with TPMS also in regions where the heat flux is not hitting the tungsten lid. This one is divided in three identic areas (numbered from 1 to 3) that simulate three different impact cases.

The tungsten lid is divided in three square areas of size $100\ mm\ \times 100\ mm$. One is near the inlet (area 1), one in the middle (area 2) and the last near the outlet (area 3).

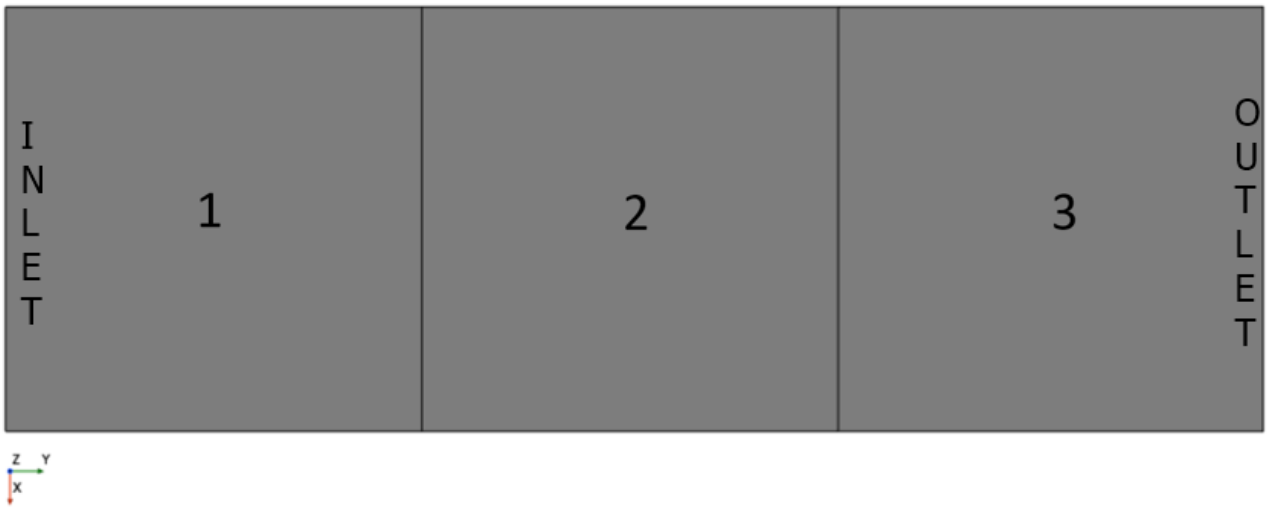

Figure 58: Three areas where the heat flux hit the target.

Area 2 and Area 3 are the most dangerous areas for boiling because they are far from the inlet. If boiling is not present in these two areas, we are pretty sure that is avoided also in Area 1. For this reason, the thermal simulations have been carried out only in Area 2 and Area 3.

To avoid the presence of boiling, the difference between the local temperature of the water and the saturation temperature at the respective local pressure must be negative.

$$Boiling\ \ if\ \ T - T_{sat} < 0$$

Area 2

The heat flux is firstly imposed in Area 2: by applying $10\,\frac{MW}{m^2}$ boiling is present only closed to the sides of the tile (Figure 59) because this region doesn't guarantee a correct circulation of water.

These are only edge effects, a simple proposal to avoid this behavior is explained in Chapter 3. The temperature of the Tungsten and Copper are well below the constraints.

To avoid boiling everywhere with the heat flux imposed in Area 2, it must be decreased to $8\,\frac{MW}{m^2}$.

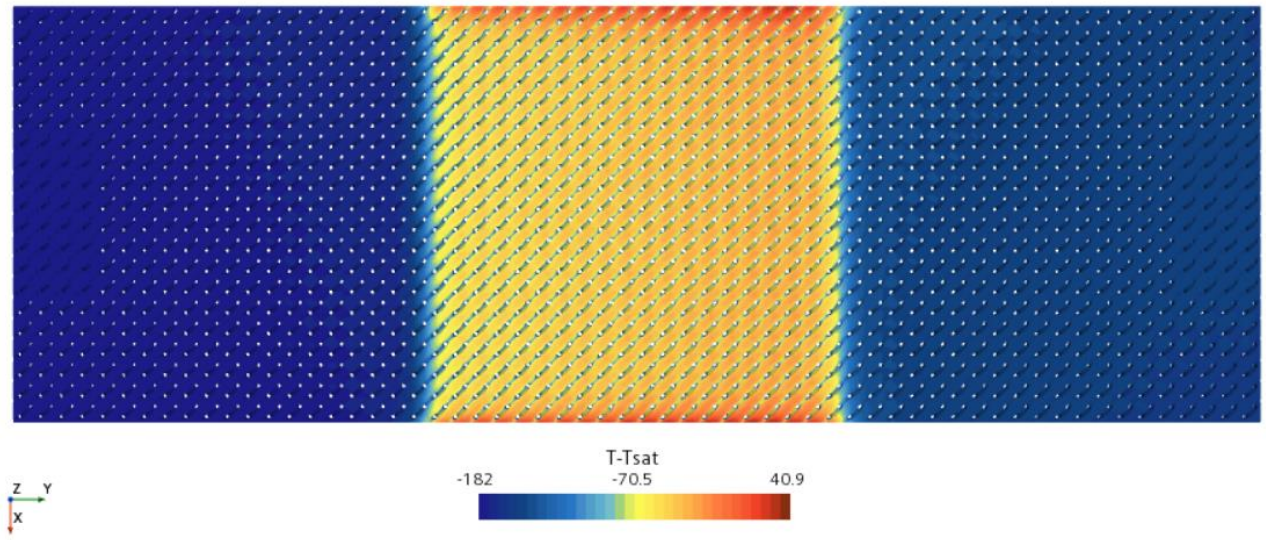

Figure 59: Check of boiling in Area 2 with a view from the top, with 10 MW/m^2 imposed.

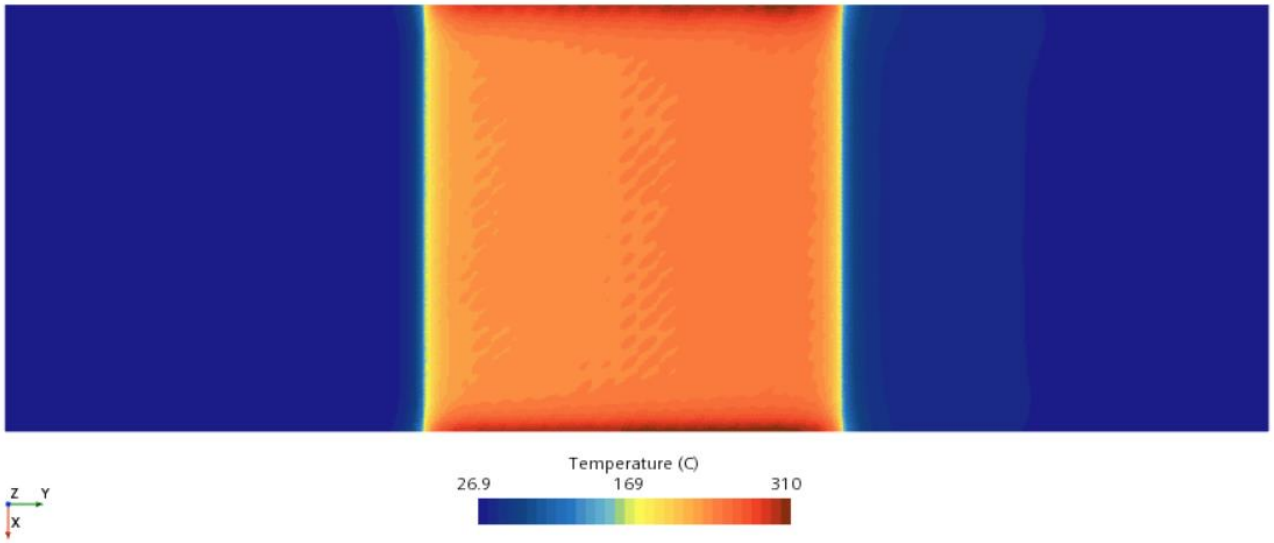

Figure 60: View from the top of Tungsten temperature in Area 2 with 10 MW/m^2 imposed.

Looking to Figure 61, with $8.0\,\frac{MW}{m^2}$ applied in Area 2, boiling is avoided everywhere. Considering the results of the small domains in Chapter 1, the tile was expected to sustain $10\,\frac{MW}{m^2}$. For this reason,

$8.0\frac{MW}{m^2}$, even if is a big heat flux, does not satisfy the ambitions. The positive aspect is that we know the regions where boiling occurs, so the design can be modified here.

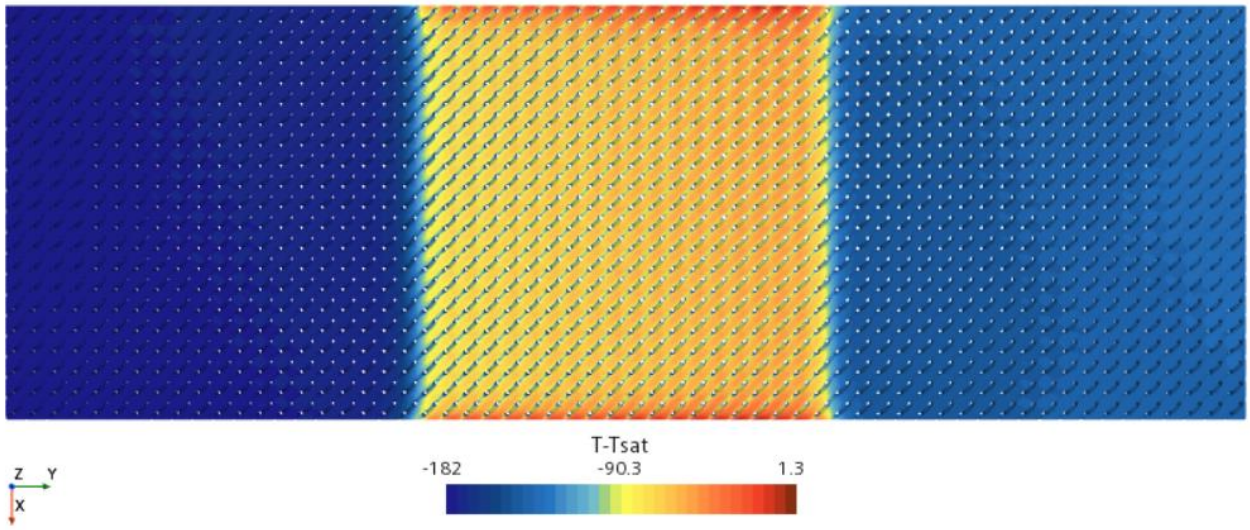

Figure 61: Check of boiling in Area 2 with a view from the top, with 8 MW/m^2 imposed.

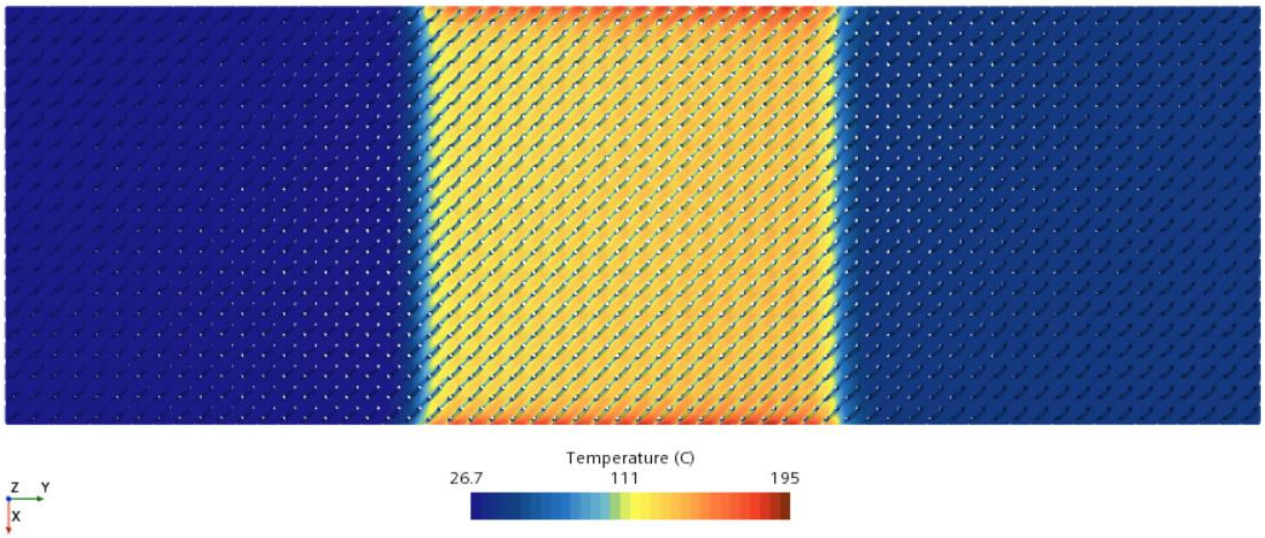

Figure 62: View from the top of Water temperature in Area 2 with 8 MW/m^2 imposed.

With $8\frac{MW}{m^2}$ applied in Area 2, the temperature of the tungsten is well below the constraints, with a maximum value of 256 [°C].

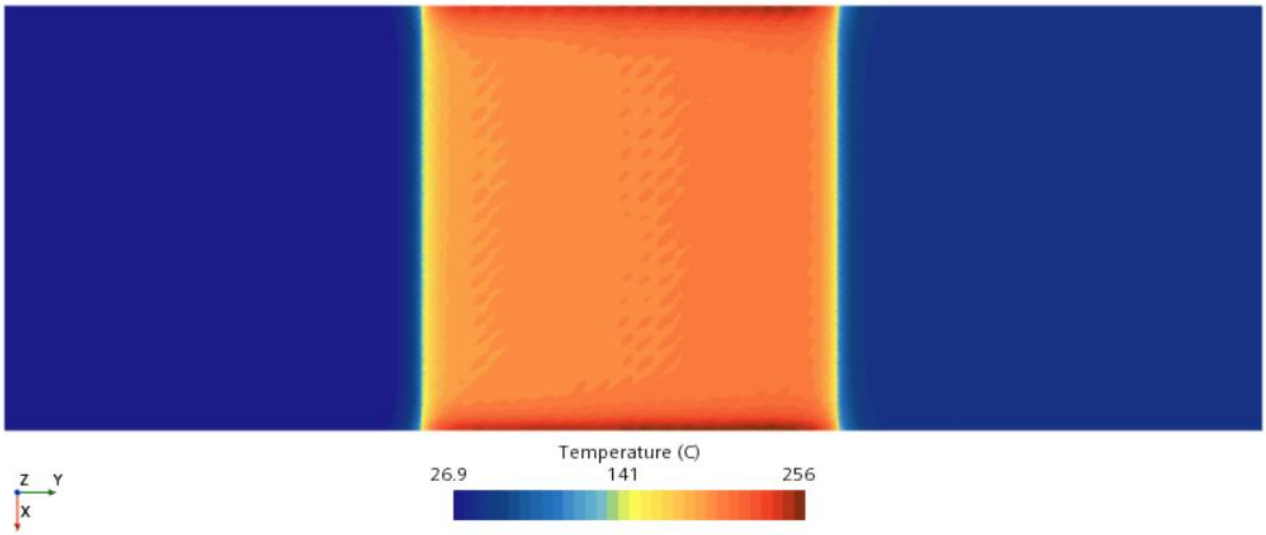

Figure 63: View from the top of Tungsten temperature in Area 2 with 8 MW/m^2 imposed.

The temperature scene on a cross section derived along the horizontal axis is shown in Figure 64. The maximum values of temperature are concentrated near the zone where the heat flux is imposed. The difference of temperature with respect to the other zones of the tile could provide thermal deformations. Fortunately, the temperature distribution on the tungsten surface tends to be symmetric (Figure 63), the situation is more dramatic considering the heat flux imposed in Area 3.

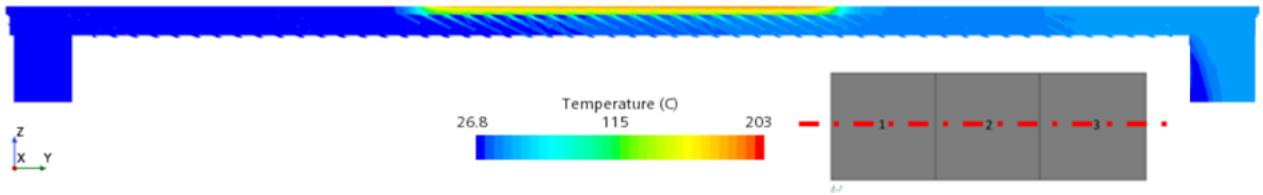

Figure 64: Global view of the temperature on a cross section along the vertical axis, with heat flux imposed in Area 2.

Area 3

Area 3 is the most dangerous for boiling problems, because of the presence of two corners and the distance from the inlet. As expected, by applying $10\frac{MW}{m^2}$, boiling is concentrated near the corners, and the temperature of the water overcomes a lot the saturation temperature. Even if the presence of boiling, the temperature of tungsten and copper are below the constraints. But if boiling occurs the flow becomes two-phase, so further investigations are needed to assess the behavior of the tile in this situation. At the moment, we can consider that such a situation during an operation would

be dramatic for the tile. In addition, looking to Figure 67, the temperature distribution on the Tungsten lid is very unsymmetric, so the tile would also feel big unsymmetric thermal stresses.

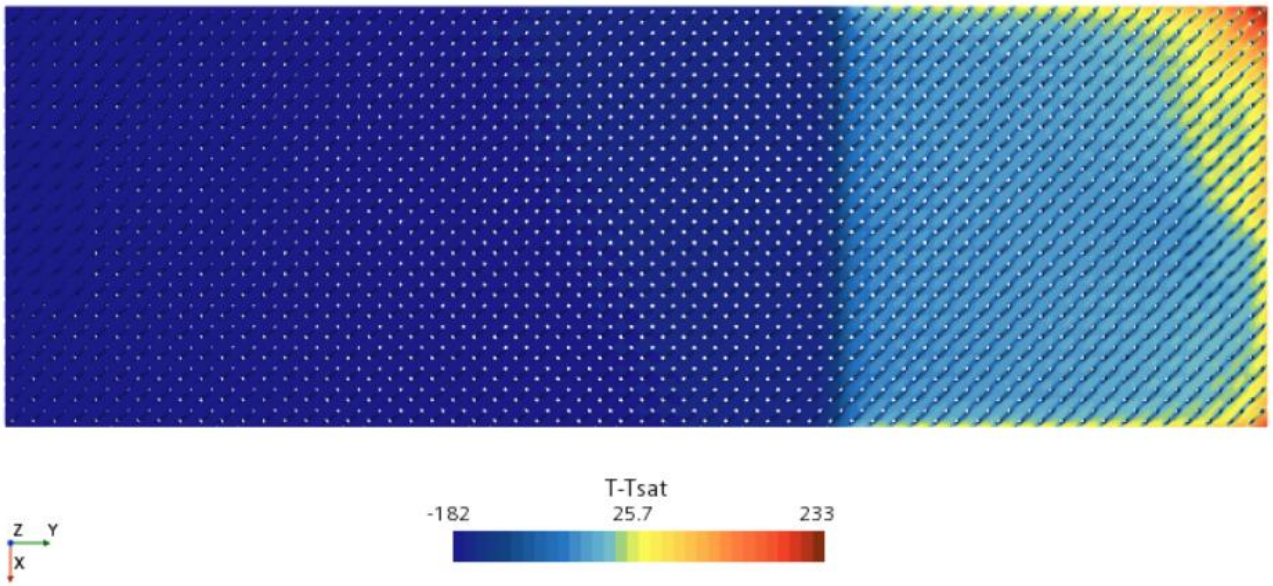

Figure 65: Check of boiling in Area 3 with a view from the top, with 10 MW/m^2 imposed.

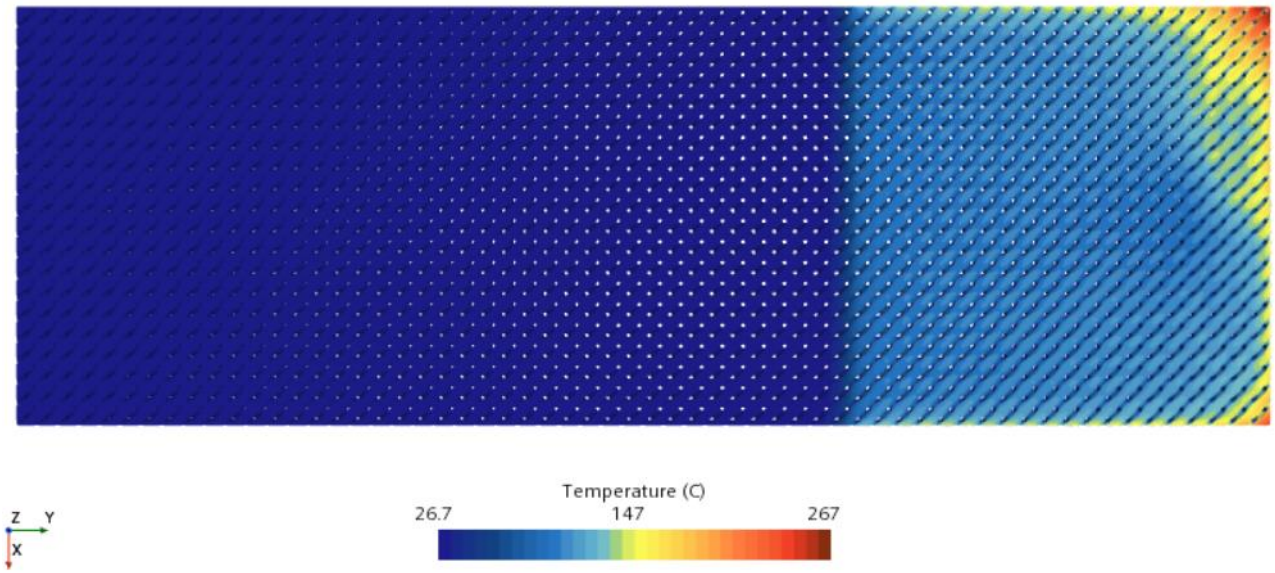

Figure 66: View from the top of Water temperature in Area 3 with 10 MW/m^2 imposed.

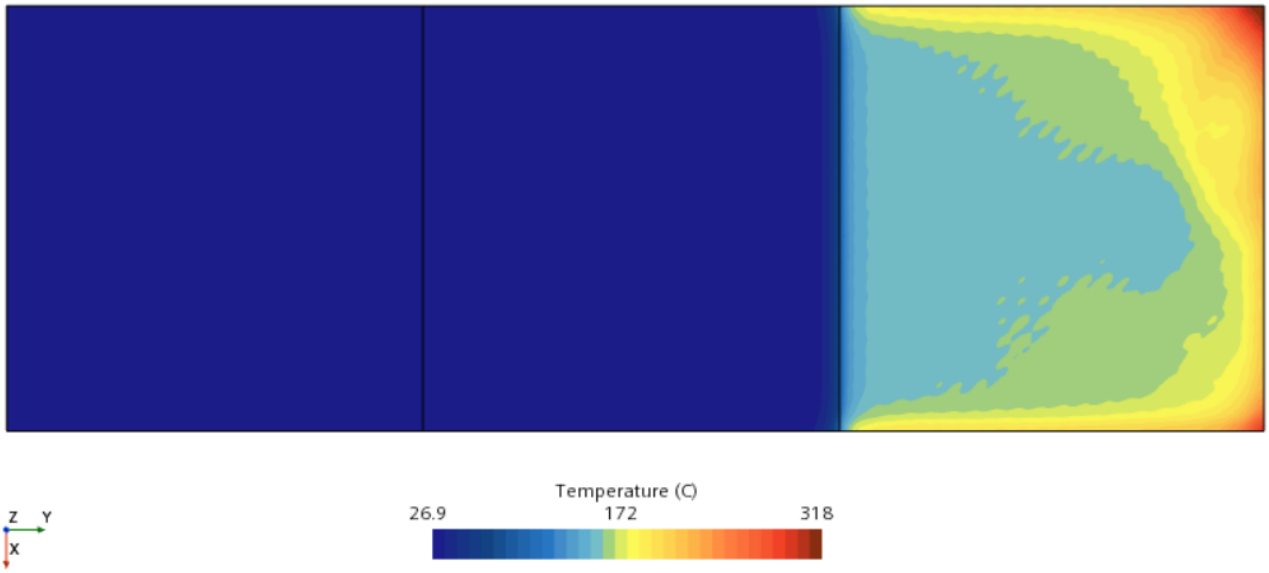

Figure 67: View from the top of Tungsten temperature in Area 3 with 10 MW/m^2 imposed.

To avoid boiling everywhere in Area 3, the heat flux must be decreased to $4\frac{MW}{m^2}$ (Figure 68), this value is well below the goal of $10\frac{MW}{m^2}$, so that design improvements will be needed in this area.

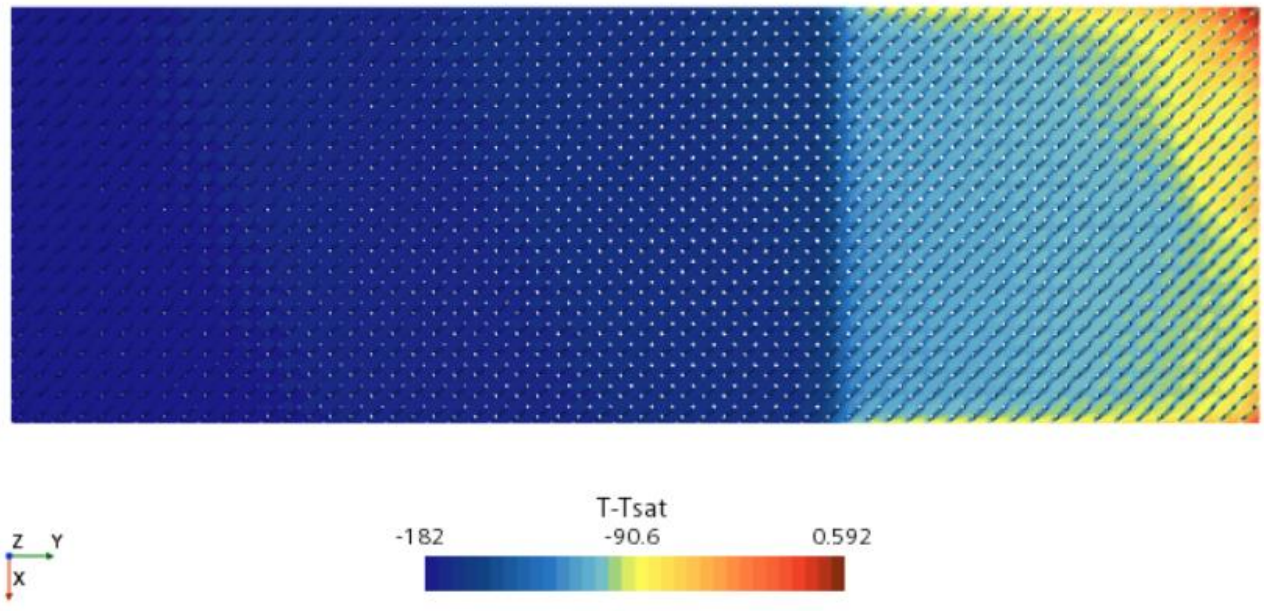

Figure 68: Check of boiling in Area 3 with a view from the top, with 4 MW/m^2 imposed.

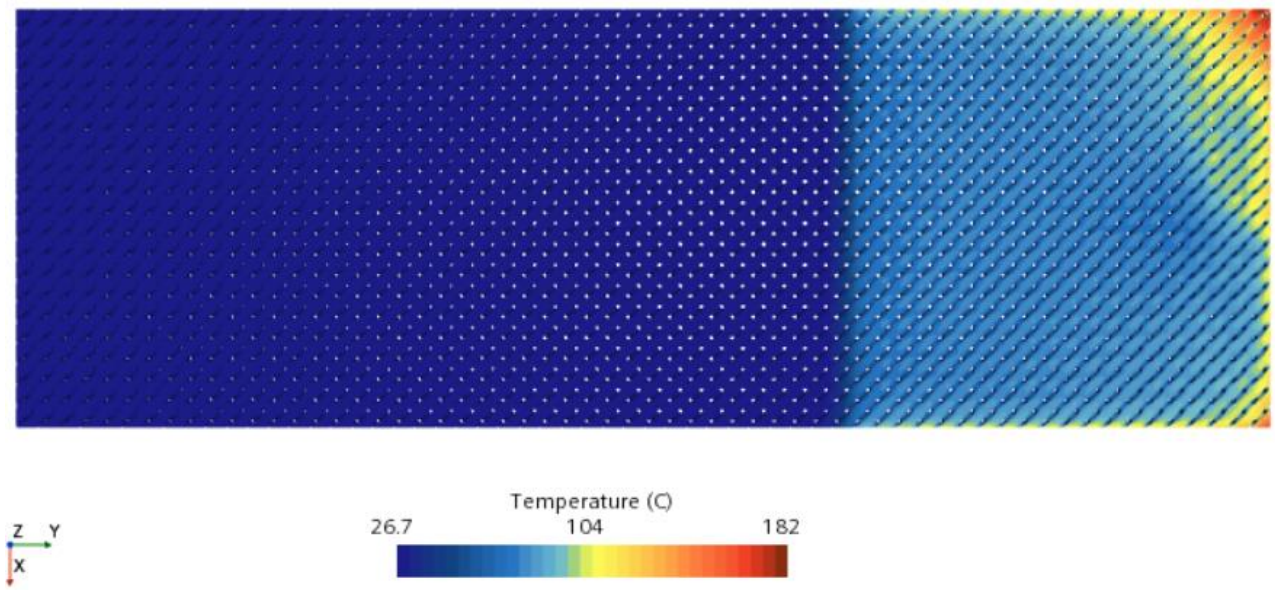

Figure 69: View from the top of Water temperature in Area 3 with 4 MW/m^2 imposed.

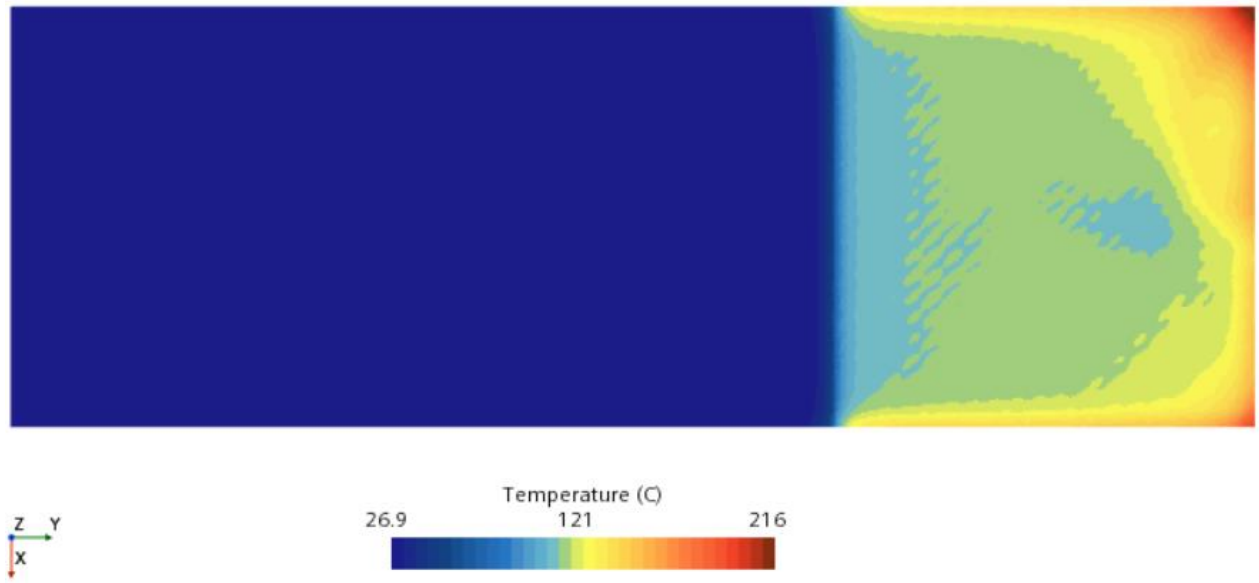

Figure 70: View from the top of Tungsten temperature in Area 3 with 4 MW/m^2 imposed.

Again, the temperature scene on a cross section derived along the vertical axis is shown in Figure 71. There is a big local hot spot in the corner, instead, most of the tile shares the same temperature. The presence of this hotspot could provide fatal thermal stresses, for this reason, in the design has been included a Soft Copper layer to avoid mismatch thermal expansions, anyway, further design modifications will be needed.

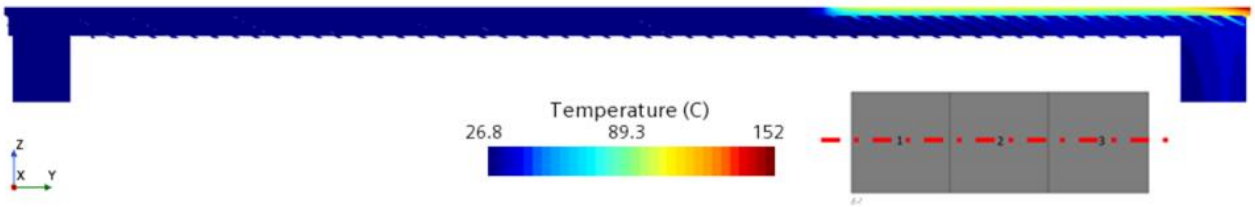

Figure 71: Global view of the temperature on a cross section along the vertical axis, with 4 MW/m^2 heat flux imposed in Area 3.

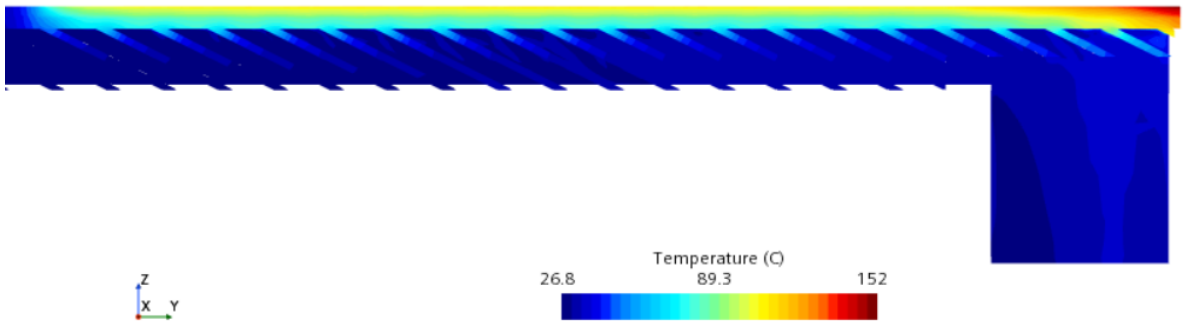

Figure 72: zoom of the global view of the temperature on a cross section along the vertical axis, with 4 MW/m^2 heat flux imposed in Area 3.

4.6 Discussion

The Schwarz Diamond has revealed as the most promising choice to be used in the Tile. It can guarantee good thermal removal capabilities and contained pressure drop. The edge and the corners of the tile are the most dangerous spots for the boiling, further developments of the design could avoid boiling also in these regions with exhausting $10\frac{MW}{m^2}$. The realization of the tile depends also on the future developments in Additive Manufacturing: the Schwarz Diamond inserted in the tile has a unit cell size of $10mm \times 10mm \times 5mm$, and it is known that there can be problems during the manufacture due to the stretched shape of the lattice. The feasibility of manufacturing lattices with this shape will be tested soon. All the simulations done in this work must be intended as a preliminary analysis, further investigations will be carried out by using temperature dependent properties for the materials.

4.7 Comparison to microchannels

Another possible solution for the divertor tile in W7-X are microchannels. They are easier to manufacture and there is more knowledge about their thermal-hydraulic behavior. The flat tile design ($100\,mm \times 100\,mm$) consists of a copper heat sink substrate and a tungsten layer that uniformly withstands the heat load. [6] The micro-channels are obtained using Additive Manufacturing techniques in a galvanized copper heat sink substrate, with tungsten as the plasma-facing material and water used for cooling. [8] The tungsten thickness is $2\,mm$. A schematic configuration is reported in Figure 73.

One tile equipped with microchannels weighs $5{,}9\ kg$.

The tile equipped with TPMS (**Error! Reference source not found.**) weighs $1{,}36\ kg$.

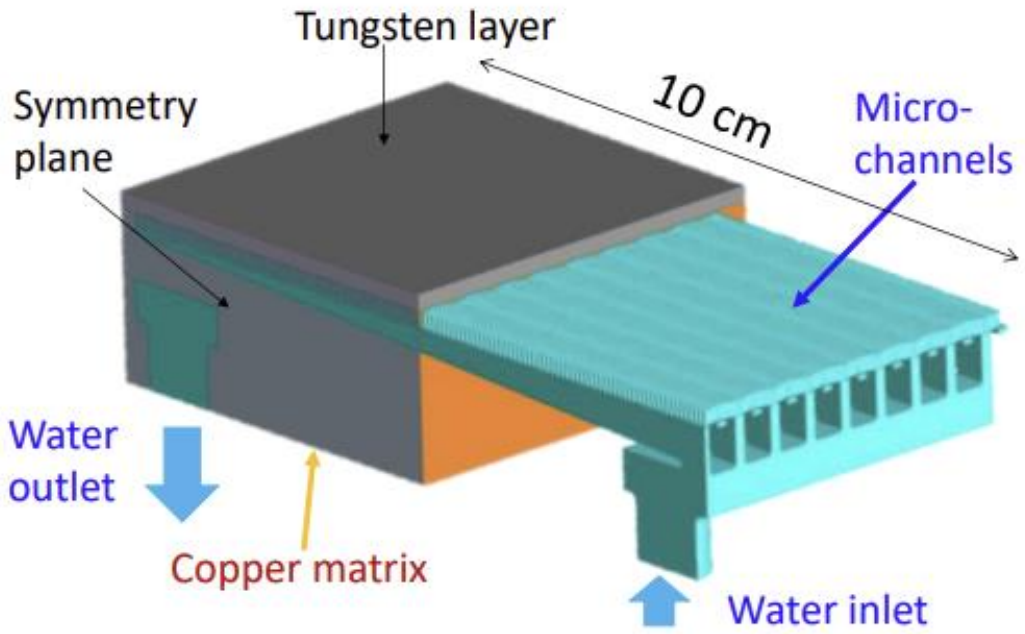

Figure 73: Tile equipped with microchannels.

The TPMSs are 80 % lighter than the microchannels, this reduction could be a determining factor in choosing the TPMS in the future design for the divertor of W7-X or other plasma devices in general.

In the following table there is a comparison of the thermal-hydraulic performances of the two tiles.

	Mass flow inlet [kg/s]	*Pressure drop [bar]*	*Heat flux max [MW/m^2]*
Microchannels tile	*1.25*	*6.1*	8.2
TPMS-based tile	*1.25*	*11*	*8 (on Area 2)* *4 (on Area 3)*

Table 24: Comparison of the thermal performances of the two tiles.

Chapter 5: Conclusions and future work

In this section is presented a possible evolution of tile (we call it '*tile v2*'), designed specifically to avoid boiling even close to the sides. As shown in Figure 74, the outlet side of the tile has been rounded to avoid the creation of temperature hotspots in the corners. The corners at the end of the tile have been rounded as well (Figure 75). *Tile v2* will be ensembled at the same way of *tile v1*: box of CuCrZr, Diamond TPMS made of CuCrZr, tungsten lid with a soft copper interlayer in between. The exploded view is shown in Figure 75.

To have a better understanding of how the tile is composed look to Figure 76.

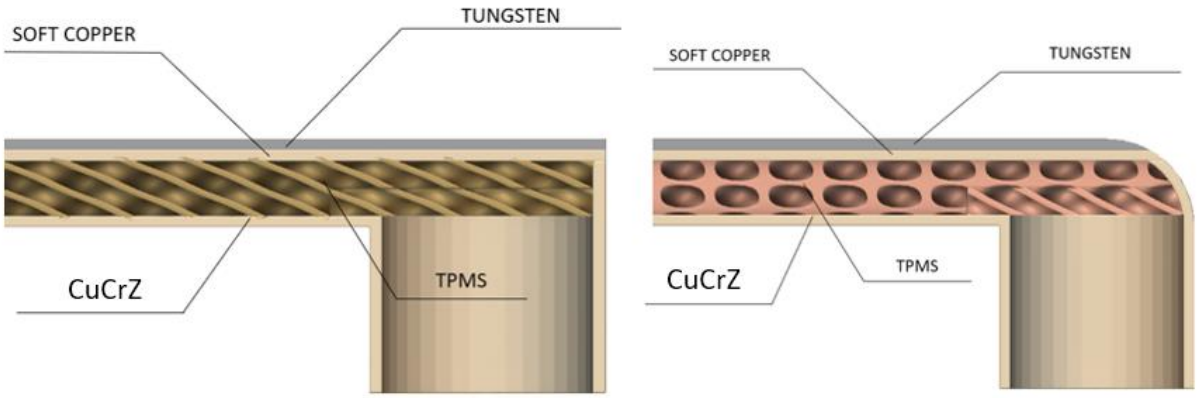

Figure 74: Comparison of the future tile end part with the present tile

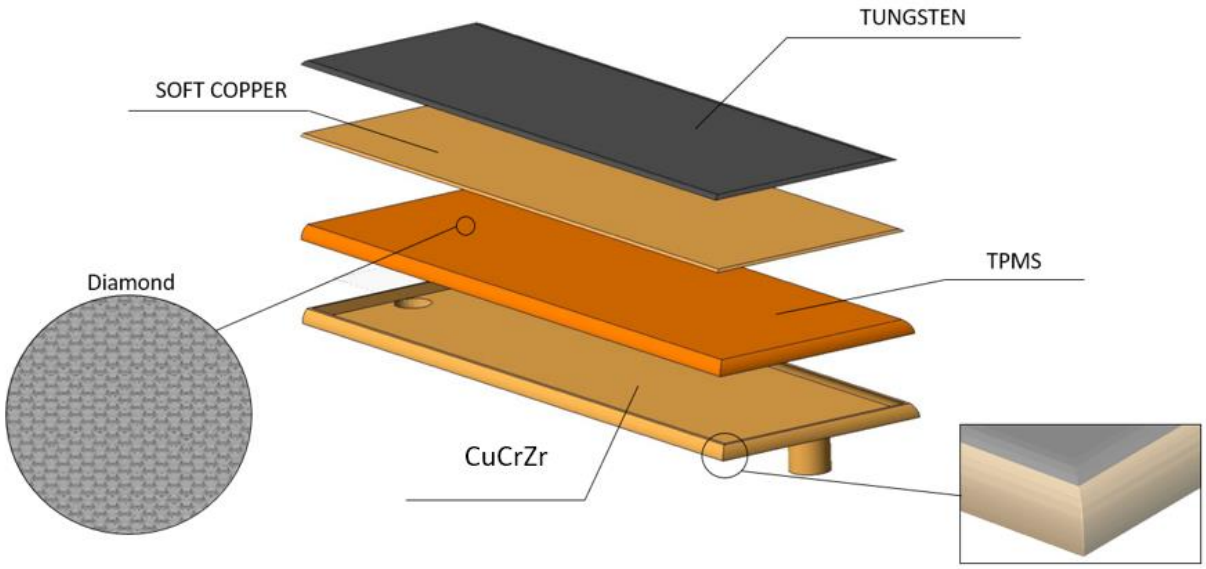

Figure 75: Exploded view of the future tile

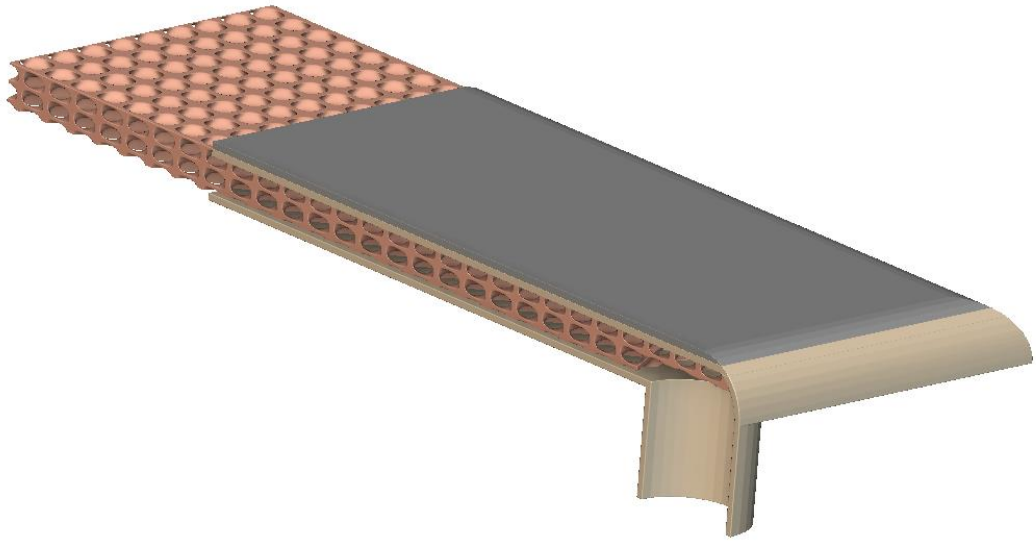

Figure 76: View of quarter of the future tile equipped with Diamond

References

1) Abousahl, S., Carbol, P., Farrar, B., Gerbelova, H. *Technical assessment of nuclear energy* . Luxembourg: Publications Office of the European Union, 2021.
2) Al-Ketan, Oraib. “Forced Convection Computational Fluid Dynamics Analysis of Architected and Three Dimensional Printable Heat Sinks Based on Triply Periodic Minimal Surfaces.” 2020.
3) Baobaid, Nada. “Fluid flow and heat transfer of porous TPMS architected heat sinks .” (n.d.).
4) Barbarino, Matteo. “Fusion Energy in the 21st Century: Status and the Way Forward.” (n.d.).
5) Boscary. “Completion of the production of the W7-X divertor target modules.” n.d.
6) Carrone Francesco, Laura Savoldi. “A multi-scale hybrid approach to the modelling and design of a novel micro-channel cooling structure for the W7X divertor.” 2023.
7) commission, European. “1) Communication from the commission to the European parliament, the council, the European economic and social committee and the committee of the regions.” 2023.
8) Ebadi. “A multi-scale hybrid approach to the modelling and design of a novel micro-channel cooling structure for the W7X divertor.” n.d.
9) energy, Fusion for. *https://fusionforenergy.europa.eu/the-device/*. n.d.
10) Fellinger, Joris. *Tungsten based divertor development for Wendelstein 7-X*. Greifswald, 2023.
11) *https://euro-fusion.org/programme/demo/*. n.d.
12) *https://www.ipp.mpg.de/w7x*. n.d.
13) IEA. “Net zero by 2050.” n.d.
14) Mechanical, American Society of. *Standard for Verification and Validation in*. n.d.
15) Pei, Eujin. *Progress in Additive Manufacturing*. n.d.
16) Siemens. *https://docs.sw.siemens.com/documentation/external/PL20211129219030255/en-US/userManual/starccmp_userguide_html/index.html#page/STARCCMP%2FGUID-44BC55FD-ACDE-47F1-A792-C904A5A45CAD.html%23* . n.d.
17) Tu, Jiyuan. “Computational Fluid Dynamics.” (n.d.).
18) White, Mary Anne. *Physical Properties of Materials, Third Edition*. 2018.
19) Zacha, Pavel. “High heat flux limits of the fusion reactor water-cooled first wall.” (n.d.).

20) Zhang, K. “Conceptual design of the next generation of W7-X divertor W-target elements.” n.d.

Appendix

Grid independence

A grid-based solution verification is used to evaluate the numerical error. Improving the grid refinement (while keeping the same number of prism layers) the solution, if it is grid independent, should tend to an asymptotic exact value. In the following we use the Richardson extrapolation [14]:

Start with defining a representative cell mesh size h:

$$h = [(\Delta x_{max})(\Delta y_{max})]^{1/2}$$

In Table 25 the number of cells, the volume and the representative cell mesh size are listed.

Base size $[mm]$	Number of cells [-]	Volume $[mm^3]$	$h[mm]$
0,5 mm	374821	2000	0.073047
1,0 mm	230422	2000	0.093165
2,5 mm	135727	2000	0.12139

Table 25: Number of cells [-], Volume [mm^3] and representative cell mesh size h [mm] for three different values of the base size.

Once h is defined, the grid refinement r is calculated as follows:

$$r = \frac{h_{coarse}}{h_{fine}} > 1/3$$

The order of convergence p can be now calculated:

$$p = \left[\frac{1}{\ln(r_{21})}\right][ln\left|\frac{\epsilon_{32}}{\epsilon_{31}}\right| + q(p)]$$

Where:

$$\epsilon_{32} = \varphi_3 - \varphi_2 \; and \; \epsilon_{21} = \varphi_2 - \varphi_1$$

φ_i is the simulation value at the i^{th} grid.

$$q(p) = \ln\left(\frac{r_{21}^p - s}{r_{32}^p - s}\right) \; with \;\; s = 1 \cdot sign(\epsilon_{32}/\epsilon_{21})$$

The order of convergence p should be comparable with the order of convergence of the discretization method used.

Then the extrapolated value can be calculated, it is the value at which the solution tends with an infinite precise mesh.

$$\varphi_{21,ext} = \ln\left(\frac{r_{21}^{p}\varphi_1 - \varphi_2}{r_{21}^{p} - 1}\right)$$

The Grid Convergence index (GCI) gives an idea about the uncertainty of the solution, the real solution can be found, with a 95% probability, in an interval of $\pm u_{num}$ range from the extrapolated solution.

$$GCI = (F_s \cdot e_a^{21})/(r_{21}^{p} - 1)$$

F_s is equal to 3, it is a conservative value recommended for unstructured grid refinement, with:

$$e_a^{21} = |\varphi_1 - \varphi_2| \; and \; u_{num} = \frac{GCI}{k}$$

$k = 2$ if the error distribution is Gaussian.

In conclusion, u_{num} is the standard uncertainty of the numerical results.

The numerical error is evaluated considering the pressure drop and the maximum temperature in the domain. All the parameters are depicted in Table 26.

	ϕ = $pressure\ [bar]$	ϕ = $T_{max}[°C]$
r_{21}	1.27	1.27
r_{32}	1.30	1.30
φ_1	9.20E-02	1.50E+02
φ_2	9.17E-02	1.53E+02
φ_3	9.13E-02	1.47E+02
p	0.83	2.70
$\varphi_{21,ext}$	0.093	146.76
$e_a^{21}(\%)$	0.33	2
$GCI\ (\%)$	1.87	2.69
$u_{num}\ (\%)$	0.93	1.34

Table 26: numerical error parameters.